**Searches For A Dark Matter Annihilation Signal With Imaging Atmospheric Telescopes**

Dissertation

zur Erlangung des akamedischen Grades

doctor rerum naturalium
(Dr. rer. nat.)
im Fach Physik

eingereicht an der
Mathematisch-Naturwissenschaftlichen Fakultät
Humboldt-Universität zu Berlin

von
**Emrah Birsin**

Präsident der Humboldt-Universität zu Berlin:
Prof. Dr. Jan-Hendrik Olbertz

Dekan der Mathematisch-Naturwissenschaftlichen Fakultät:
Prof. Dr. Elmar Kulke

Gutachter:
1. Prof. Thomas Lohse
2. Prof. Marek Kowalski
3. Prof. Markus Boettcher

**Tag der mündliche Prüfung: 24.3.2015**

"For something to exist, it has to be observed. For something to exist, it has to have a position in time and space. And this explains why nine-tenths of the mass of the universe is unaccounted for. Nine-tenths of the universe is the knowledge of the position and direction of everything in the other tenth... Nine-tenths of the universe, in fact, is the paperwork."

*Terry Pratchett, Thief of Time*

**Abstract**

First indications for the existence of Dark Matter appeared in 1933. The astrophysicist Fritz Zwicky observed the velocity dispersion of the Coma Cluster and found out that 400 times the visible mass must be contained in the galaxy cluster or the cluster could not be gravitationally bound and would disperse.
Despite extensive efforts over the last 80 years not much is known about Dark Matter. The facts known are that Dark Matter interacts via gravitation, does not interact electromagneticly and is the main constituent of matter. But current experiment searching for Dark Matter directly and indirectly begin to reach sensitivities that can probe interesting parameter spaces for Dark Matter candidates like the lightest supersymmetric particle, meaning the first Dark Matter detections could happen in the near future.
In this thesis a dwarf stacking analysis for Dark Matter signal search using H.E.S.S. data is performed and a upper limit is calculated. Furthermore the prospect for a Dark Matter search with CTA in the galactic center region of the Milky Way is presented for different candidate arrays and different annihilation channels. The results will show that CTA will be able to reach velocity annihilation below $3 \cdot 10^{-26}\,\mathrm{cm^3 s^{-1}}$, the velocity annihilation cross-section expected for a weakly interacting Dark Matter particle, within 100 h of observation which can reasonably be acquired within one to two years.

## Zusammenfassung

Erste Anzeichen für die Existenz von Dunkler Materie wurden 1933 entdeckt. Der Astrophysiker Fritz Zwicky beobachtete die Geschwindigkeitsverteilung im Coma Cluster und fand dabei heraus, dass 400 mal mehr Materie im Galaxie Haufen sein muss, damit dieser gravitativ gebunden sein kann oder der Galaxie Haufen würde sich auflösen.
Trotz erheblicher Bemühungen über die letzten 80 Jahre ist nicht viel über Dunkle Materie bekannt. Das einzige was man weiß ist, dass Dunkle Materie gravitativ aber nicht elektromagnetisch wechselwirkt und Dunkle Materie stellt den größten Bestandteil der Materie im Universum da. Doch derzeitige Experimente die nach Dunkler Materie suchen, sowohl direkte Suchen als auch indirekte, beginnen sensitiv genug zu werden um interessante Parameterbereiche von Dunkle Materie Kandidaten zu untersuchen wie das leichteste Super-symmetrische Teilchen, was bedeutet, dass die Entdeckung von Dunkler Materie in der nahen Zukunft sein könnte.
In dieser Arbeit wird eine Signalsummierung von H.E.S.S. Zwerg Galaxien Daten durchgeführt und obere Ausschlussgrenzen berechnet. Weiterhin wird die Leistung einer Dunklen Materie Suche im galaktischen Zentrum durch CTA präsentiert für verschiedene mögliche Teleskop Anordnungen und verschiedene Annihilation Kanäle. Die Ergebnisse werden zeigen, dass CTA in der Lage sein wird geschwindigkeitsgemittelte Annihilations Wirkungsquerschnitte von $3 \cdot 10^{-26}\,\mathrm{cm^3 s^{-1}}$ und geringer, der geschwindigkeitsgemittelte Annihilations Wirkungsquerschnitt der für schwach wechselwirkende Dunkle Materie erwartet wird, in 100 h zu erreichen. Diese Beobachtungszeit kann innerhalb von ein bis zwei Jahren erreicht werden.

# Contents

# Chapter 1

# Introduction

First indications for the existence of Dark Matter (DM) appeared in 1933. The astrophysicist Fritz Zwicky observed the velocity dispersion of the Coma Cluster and found out that 400 times the visible mass must be contained in the galaxy cluster or the cluster could not be gravitationally bound and would disperse.
Over time more and more evidence was found in astronomical objects ranging from galactic scales up to cosmological scales. Today DM is a well accepted idea. It is known that around 84.6% of all matter in the Universe consists of DM meaning that DM is more important for structure formation and evolution of the Universe than ordinary matter.
Despite extensive efforts over the last 80 years not much is known about DM. The facts known are that DM interacts via gravitation, does not interact electromagneticly and is the main constituent of matter. But current experiment searching for DM directly and indirectly begin to reach sensitivities that can probe interesting parameter spaces for DM candidates like the Lightest Super-Symmetric Particle (LSP), meaning the first DM detections could happen in the near future.
Furthermore the Large Hadron Collider (LHC) began operation in 2010 with a center of mass energy of 7 TeV. In the proton-proton collisions DM could be produced and would lead to high missing energy in the events. Currently (2013) LHC is in a shutdown for an upgrade. After the upgrade LHC will reach center of mass energies of 14 TeV and will be able to probe a wider parameter space of DM candidates. But even if LHC detects a possible candidate particle LHC will not be able to prove that the particle is indeed DM, here direct and indirect experiments will still be needed.
This thesis is structured as follows. In Section 2 first some evidence for the existence of DM will be presented followed by a list of candidates and after that an explanation of some experiments designed to directly and indi-

rectly detect DM. In Section 3 the detection technique used in ground-based gamma-ray astronomy is described with the current High Energy Spectroscopic System (H.E.S.S.) experiment and the future Cherenkov Telescope Array (CTA) as examples. After these introductory sections DM searches with H.E.S.S. and CTA are presented in the chapters 4 and 5, respectively. Appendix A explains the details of the parameter optimization needed for the analysis in Chapter 4.
In appendix B the work done by the author on the CTA Medium Sized Telescope (MST) prototype, namely the integration of a weather station, is described. This includes the implementation of communication between the CTA array control software and an OPC UA server and data storage in a MySQL data base. As regards content the Appendix B is separated from the physics discussed in this thesis.

# Chapter 2

# Dark Matter

DM accounts for 24% of the mass-energy-budget and 84.6% of the matter in the Universe. Although DM is the most abundant form of matter it is not known what the nature of DM is. Determining the nature of DM is one of the most important issues in astronomy and particle physics today.
This chapter introduces evidence of DM and the known properties of DM. After that a short introduction into direct and indirect DM searches is presented.

## 2.1 Evidence for Dark Matter

This section contains a small and by far not complete list of evidence for the existence of DM from astrophysics and cosmology. For a more in depth description see [1] and references in there.

**Galaxy clusters**

In 1933 Fritz Zwicky observed the velocity dispersion of galaxies in the Coma galaxy cluster [2]. Assuming that the cluster is stable and using the viral theorem he estimated that the cluster must be 400 times more massive than the visible mass suggests.
In recent times gravitational lensing strengthened Zwicky's results [3]. Furthermore gravitational lensing allowed to make DM "visible" in colliding galaxy clusters like 1E0657-558 (also known as the bullet cluster) [4]. In the collision the intergalactic plasma is separated from DM. The intergalactic plasma contains the majority of the baryonic mass in the galaxy cluster, but when probing the mass distribution with gravitational lensing the center of mass is reconstructed at the position of the stars because like the stars DM is collisionless and did therefore not separate from its host galaxies and DM

accounts for far more mass than the intergalactic gas.

**Galaxy rotation curves**

The most commonly known proof for the existence of DM are rotation curves of galaxies. By measuring the Doppler shift of stars and hydrogen gas a velocity profile of the galaxy can be obtained. For a gravitationally bound object the velocity is given by

$$V(R) \propto \sqrt{\frac{M(R)}{R}}, \tag{2.1}$$

where $V(R)$ is the velocity as a function of the distance $R$ to the galaxy center and $M(R)$ the mass contained in the radius $R$. While the inner parts of the profile depends on the structure inside the galaxy and is difficult to predict, the profile that extends beyond the visible part of the galaxy is easy to predict. At large radii, where the mass does not increase significantly any more the Equation (2.1) simplifies to:

$$V(R) \propto \sqrt{\frac{M_{galaxy}}{R}} \propto R^{-0.5}.$$

Every velocity profile of any galaxy should start to fall as $R^{-0.5}$ independent on the inner structure. But actual measurements like seen in Figure 2.1 (extracted from [5]) show that the velocity stays constant far beyond the visible part of the galaxy. The dashed line in the figure shows the expected rotation velocity as derived from the visible mass. The dotted line shows the contribution of interstellar gas. Both components together can not explain the shape of the rotation curve, a dark halo (indicated by the dashed dotted line) must be introduced. The flat rotation curve could in principle be explained by Modified Newtonian Dynamics (MOND) theories, extensions of the theory of gravitation which modify the gravitational force at higher distances. But MOND theories can not explain results from colliding galaxy clusters, see above, and results from Cosmic Microwave Background (CMB) measurements, see below. Therefore a DM halo around galaxies is postulated.

**Cosmic Microwave Background**

After the Big Bang the Universe was opaque for photons because the electrons and protons had kinetic energies so high that they could not form bound states and could therefore easily absorb any photon regardless of the photon energy. Due to the cosmic expansion the electrons lost energy until

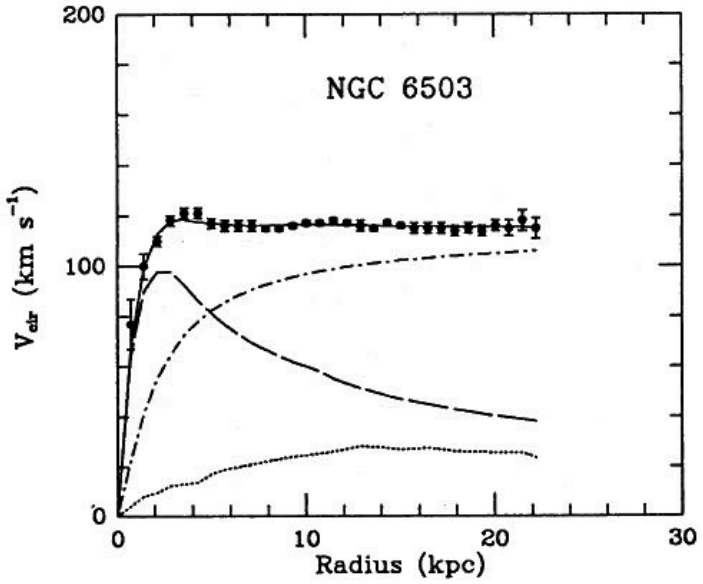


**Figure 2.1:** Rotation curve of the galaxy NGC 6503. The star's velocity does not decrease at high distances from the galaxies center as the luminous matter would suggest (dashed line) but instead stays constant after $\approx 3\,\mathrm{kpc}$. This behavior can be explained by introducing a dark halo around the galaxy, indicated by the dashed dotted line. The dotted line shows the contribution of interstellar gas. Figure extracted from [5].

the energy was lower than the bounding energy of hydrogen, leading to the formation of hydrogen and the decoupling of the photons. The photons of that time propagated through the Universe and were red-shifted by the cosmic expansion to the Microwave regime. These photons are known as the CMB.

Many cosmological parameters left imprints on the temperature fluctuations of the CMB as shown in [6]. Two interesting parameters for DM are $\Omega_m h^2$ the energy density of mass in the Universe and $\Omega_b h^2$ the energy density of baryonic matter. In absence of DM both numbers should be equal. Recent results by the Plank satellite [6] yield

$$\Omega_b h^2 = 0.02205 \pm 0.00028$$

$$\Omega_m h^2 = 0.1426 \pm 0.0025.$$

$\Omega_m h^2$ is by a factor of around 6.5 lager than $\Omega_b h^2$ making it clear that baryons are only the tip of the iceberg.

Moreover from CMB data combined with N-body simulations and large-scale structure observations we know that DM must be "cold" meaning that

DM particles had non-relativistic speed when they dropped out of thermal equilibrium. For this kind of DM candidates the relic density at freeze-out can be expressed as

$$\Omega_\chi h^2 \propto \frac{3 \cdot 10^{-27}\,\mathrm{cm}^2/\mathrm{s}}{\langle \sigma_{anni} v \rangle} \tag{2.2}$$

giving a rather strict prediction on the DM's velocity weighted annihilation cross-section $\langle \sigma_{anni} v \rangle$. This prediction is important because it gives a strong expectation value for DM annihilation cross-section.

## 2.2 Dark Matter Candidates

Over the years many different candidates were considered. Obvious candidates like Massive Compact Halo Objectss (MACHOs), e.g. brown dwarfs, black holes and neutron stars that can not be directly observed could not explain DM [7]. Even modifications of the gravitation theory like MOND theories [8] were considered. MOND theories modify the strength of gravity at large distances. While MOND can explain galactic rotation curves it can not explain other effects of DM, see previous section.
Neutrinos produced in the Big Bang are known to contribute to the DM content of the Universe. But with a mass $< 2\,\mathrm{eV}$ [9] neutrinos had relativistic speeds when they dropped out of thermal equilibrium in the early Universe making them "hot" DM. As explained in the last section DM must be cold to explain the observed large structure formation, so neutrinos can not constitute a significant amount to the DM content.
Over time many more candidates were excluded. Two still promising candidates, but not the only ones left, are Axions and Weakly Interacting Massive Particles (WIMPs).

### Axions

Axions were introduced to solve the strong CP problem [10]. While in principle CP violation could appear in strong interactions, until today it was not observed. To explain the absence of CP violation in the strong interaction a scalar field can be postulated which introduces a new particle, the axion. Axions can convert to photons in a magnetic field and vice versa. Axions are expect to have masses in the order of keV [11] making it impossible for Cherenkov telescopes to measure any signal directly from axions. But because photons can convert into axions and vice versa, the existence of axions

could be shown by their imprint on the gamma-ray spectra of astrophysical sources such as blazars [12, 13].

#### WIMPs

Weakly Interacting Massive Particles (WIMPs) are actually not a specific particle species but a class of particles. As the name suggests WIMPs interact via the weak force and are massive, so massive that they contribute to cold DM. Additionally, typical annihilation cross-sections for weakly interacting particles are around $10^{-26}\,\mathrm{cm}^3/\mathrm{s}$ meaning the relic density for WIMPs is, according to Equation (2.2), is in the right order of magnitude to explain the CMB structure. This coincidence is known as the WIMP miracle.
But the most important aspect about WIMPs with respect to DM is that extensions of the Standard Model (SM) like Supersymmetry (SUSY), that try to answer problems the SM can not answer and were not introduced to explain DM, predict new weakly interacting massive particles that are stable, or have a half life in the order of the age of the Universe, like the LSP. These new particles are perfect WIMP candidates that could be detectable for Cherenkov telescopes. In the remainder of this thesis it is assumed that DM consists of WIMPs.

## 2.3 Direct Searches for Dark Matter

Direct DM searches are trying to observe collisions of DM particles with normal matter. To detect the few expected DM events a huge background must be suppressed. Therefore direct detection experiments are based deep underground to reduce background induced by cosmic rays. Shielding further reduces background stemming from cosmic rays and ambient radioactivity. Furthermore materials used in the experiment must be as clean of radioactive isotopes as possible.
But still SM particles can reach the detector, especially neutrinos and muons. To discriminate DM events from normal events the experiments take different approaches. Atoms hit by DM or other particles can produce, depending on the medium, ionization, phonons and scintillation. The energy deposited in the three signatures depends on the incident particle. By using correlation between two measured properties background events can be excluded.
Here, two of this experiments should be mentioned as examples. For a more in-depth review of direct experiments see [14].

### XENON100

XENON100 is a dual phase Time-Projection Chamber (TCP) equipped with 242 Photo Multiplier Tubes (PMTs) at the Gran Sasso underground laboratory using 100 kg of liquid xenon as target material [15]. The signal consists of two parts. An interaction in the xenon creates a prompt scintillation signal (S1) and ionizes atoms. The ions drift through the TCP and produce a secondary scintillation signal in the gas phase (S2). The ratio $S1/S2$ is sensitive to the interaction type and is used to discriminate hadronic interactions from electro-magnetic interactions. Furthermore the position of the interaction vertex can be reconstructed to exclude events close to the detector walls which are most likely induced by radioactivity in the surrounding materials. The recent upper-limits for spin-independent interactions from XENON100 can be seen in Figure 2.2. Shown are also limits from other experiments including the results of the Dark Matter (DAMA) experiment, see next paragraph. The grey area in the figure denotes the Constrained Minimal Supersymmetric Extension of the Standard Model (cMSSM) parameter space. As can be seen XENON100 starts to probe the interesting parameter space. XENON100 will be soon upgraded to XENON1t (increasing the target material from 100 kg to 1 t) and will then probe the SUSY parameter space even further.

### DAMA Experiment

DAMA has a different approach to background suppression. Instead of discriminating the background events DAMA searches for a modulation of the event rate over the year due to the relative motion of the Earth around the sun to the motion of the solar system around the galaxy [16]. This movement should lead to a yearly modulation of the event rate. DAMA has found such a yearly modulation in its data [16]. The resulting spin-independent cross-section can be seen in Figure 2.2. The problem with the result is, that the signal region of DAMA is already excluded by other more sensitive experiments.
A possible explanation that can reconcile the different experimental results is that the interaction is spin-dependent [17, 18]. In that case DAMA would be more sensitive and other experiments would not have excluded the signal region. The interpretation of the DAMA results is strengthened by CoGeNT [19] a similar experiment searching for a yearly modulation of event rates. Still the results are not conclusive and are under debate. It will take further investigations to reach conclusion. Cherenkov telescopes will probably not be able to help solving the contradictions due to the low implied

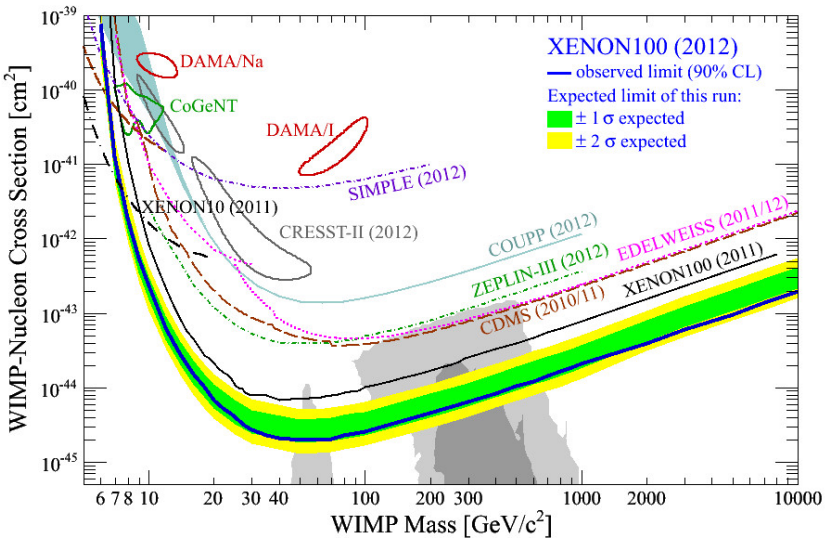


**Figure 2.2:** Spin-independent WIMP-Nucleon cross section limits for several direct DM searches. The best XENON100 limit is compared to limits from several other limits, including DAMA. The gray areas denote the parameter space of the cMSSM that is still in accordance with searches at the LHC. Figure extracted from [15].

mass of around 10 GeV.

## 2.4 Indirect Searches for Dark Matter

Indirect DM searches are looking for secondary particles produced in a DM annihilation or decay. Interesting messenger particles are positrons, anti-protons, neutrinos and photons.
Due to the galactic magnetic fields charged messenger particles travel on bent trajectories. Therefore the origin of the particles can not be reconstructed but the annihilation products could lead to an excess over the diffuse background flux. Such an excess was found by the PAMELA satellite [20] in the positron flux. The result was confirmed by the FERMI satellite [21]. The excess can be interpreted as a 3 TeV DM particle mainly annihilating into $\tau^+\tau^-$ with an annihilation cross-section of $2 \cdot 10^{-22}\,\mathrm{cm}^3/\mathrm{s}$ [22]. For a thermal DM particle the annihilation cross-section is quite high disfavoring the DM interpretation. Furthermore the uncertainties on the background model for cosmic rays are high and there are astrophysical explanations. For example a nearby pulsar could also produce the positron excess [23].
Neutral particles have the advantage that they are propagating on straight

paths and the source can be reconstructed readily.
Due to the weak interaction of neutrinos they reach Earth without absorption but for the same reason neutrino detectors like IceCube [24] or Antares [25] have to cover huge volumes to be sensitive enough .
The last, and for this work the most important, messenger particle that will be mentioned here is the photon. The annihilation reaction

$$\chi + \chi \rightarrow \gamma + \gamma$$

leads to a mono-energetic gamma-ray line with a photon energy corresponding to the DM mass, a smoking gun signature. Unfortunately DM does not directly couple to photons and therefore the reaction is loop-suppressed, but noteworthy Fermi observed a line-like excess at around 130 GeV [26]. The nature of the 130 GeV excess is still under study.
Another promising strategy is to look for a continuous gamma-ray spectrum with a cut-off at the DM mass. In this case the photons are not directly produced but are created as secondary products by fermions and bosons originating from the annihilation. Assuming a photon spectrum $\frac{dN_\gamma}{dE}$ and a velocity averaged annihilation cross-section $\langle \sigma v \rangle$ the annihilation flux can be expressed as:

$$\frac{d\phi_\gamma}{dE} = \frac{1}{8\pi} \underbrace{\frac{\langle \sigma v \rangle}{M_\chi^2} \int_0^{M_\chi} \frac{dN_\gamma}{dE} dE}_{\text{Particle Physics Factor}} \underbrace{J\left(s, \Omega\right)}_{\text{Astrophysical Factor}} . \tag{2.3}$$

The first part is the particle physics factor and depends on the specific DM model used. Especially the photon spectrum $\frac{dN_\gamma}{dE}$ is sensitive to the DM model. For this annihilation spectrum used in this work results of [27, 28] were used. Furthermore it is assumed that DM only annihilates into one channel. An important feature all annihilation spectra of DM have is, that no photons with energies above the DM mass are produced because all DM in the Universe is expected to have small kinetic energies. This means the spectra have a sharp cut off at the DM mass which is not expected for astrophysical gamma-ray sources.
The second factor is the astrophysical factor that only depends on the distribution of DM in the observed solid angle $\Delta\Omega$. As discussed in the next paragraph the astrophysical factor plays an important role in the selection of interesting objects for DM searches.
The astrophysical factor $J$ is the only factor in Equation 2.3 that depends on the observed target and is defined as the line of sight (los) integral in the signal region $\Delta\Omega$ over the DM particle density squared:

$$J = \int_{\Delta\Omega} d\Omega \int_{los} ds \; \rho_\chi^2(s, \Omega).$$

Due to the square dependence of J on the DM density the expected signal is strongly dependent on the density making objects with high expected DM densities more important than objects with higher over all DM content.
The DM halos of the Milky Way and of dwarf galaxies are expect to have high DM densities in the central regions, but obtaining $J$ for the inner parts of galaxies or dwarf galaxies is not trivial. One way to deduce the DM density is to measure the velocity of stars in the object. Together with measured gas and star distributions the DM content can be reconstructed. Dust clouds, which tend to be abundant in the central regions of galaxies, absorb light which makes the analysis more complicated. Also only the velocity component parallel to the line of sight is measurable introducing ambiguities.
Another way to estimate $J$ is to use large N-body simulations. In N-body simulations the large scale structure formation in the Universe is simulated starting from the small density fluctuations seen in the CMB. Because dark energy and DM account for $\approx 95\%$ of the Universe energy Baryons are not included in the simulations due to the small impact on large scale structures, but on small scales, like halo cores, baryons are more important and can modify the DM distribution. For example adiabatic contraction can enhance the central regions [29] while super nova tend to delude the DM concentration in central regions of a halo [30].
The results of the large N-body simulations fit well with observed large scale structures in Galaxy Redshift Surveys like 6dF [31]. A remarkable result of the simulations is, that there seems to be a general density profile for all DM halos. Older simulations [32, 33] tended towards the Navarro-Frenk-White (NFW) profile

$$\rho(r) = \frac{\rho_s}{\left(\frac{r}{r_s}\right)\left(1+\frac{r}{r_s}\right)^2} \tag{2.4}$$

with the scaling parameter $r_s$. The problem with the NFW profile is, that it diverges at $r = 0$. Newer simulations favor the Einasto profile [34]

$$\rho(r) = \rho_{-2} \exp\left(-\frac{2}{\alpha}\left[\left(\frac{r}{r_{-2}}\right)^{\alpha} - 1\right]\right) \tag{2.5}$$

which flattens towards $r = 0$ and reaches a finite value. For a more detailed review on DM halo profiles see [35].
In this work two different sources are used to get a $J$ estimate. For the dwarf galaxy stacking the used astrophysical factor was extracted from the velocity dispersion of stars in the dwarf galaxy by G. Martinez [36]. For the DM halo studies result of the Aquarius N-body [37] simulation were used.

# Chapter 3

# Gamma-Ray Astronomy

In 1912 Victor Franz Hess discovered that highly energetic particles from space, Cosmic Rays (CRs), hit the Earth's atmosphere [38]. Philip Morrison reviewed the prospect of high energy gamma-rays from neutral pion decay and synchrotron radiation in astronomical objects in 1958 [39]. The Explorer 11 satellite measured for the first time cosmic gamma-rays in 1961 [40]. Finally in 1989 the first ground based gamma ray source detection by the Whipple telescope was announced [41].
Today gamma-ray astronomy is a well established research field. More than 100 sources are known with some source types identified. Though this thesis concentrates on DM searches a short introduction into classical astrophysical gamma-ray sources will be given in this section to provide a background.

## 3.1 Sources Of Gamma-Rays

Very High Energy ($E \geq 100\,\mathrm{GeV}$) (VHE) gamma-rays are believed to be a secondary product, generated by primary CRs. Protons and heavier nuclei can produce gamma-rays via hadronic interactions with the Inter Stellar Medium (ISM) where neutral pions will be produced which decay into two photons. Electrons can produce gamma-rays via Inverse Compton (IC) scattering where low energy photons (for example from the infra-red background light or a local radiation field) are up scattered to gamma-ray energies.
The acceleration mechanism for the primary CR is not certain but diffusive shock acceleration [42] is widely believed to be the main mechanism. In this model particles are accelerated by crossing a shock front multiple times gaining energy every time.
Following is a short description of some known gamma-ray sourc types. This list is by no means complete. For a more in depth review see [43].

### Gamma Ray Bursts

Gamma-Ray Bursts (GRBs) are brief flashes of high energy photons. GRBs were first observed in 1973 by the Vela satellite. For a long time most explanation considered GRBs to be of galactic origin due to the high luminosity of GRBs. In 1997, the BeppoSAX satellite [44] was able to associate a GRB with a galaxy [45]. It became clear that GRBs are the most luminous single events known, even detectable on cosmological scales. It is believed that the emission is focused in two beams emitted back-to-back because an isotropic energy release would be incredible high. For example, the GRB "GRB 080916C" would have had an isotropic energy release of $E_{iso} \approx 8.8 \cdot 10^{54}\,\text{ergs} = 8.8 \cdot 10^{47}\,\text{J}$ in the emitted in the energy range from 10 keV up to 10 GeV [46] which corresponds to approximately 4.5 times the sun's mass released in energy within seconds.
Today GRBs are classified into to groups, short and long GRBs. Short GRBs last not longer than 2 s. It is believed, that short GRBs are due to a neutron star merging with an other compact object like another neutron star or black hole.
GRBs longer than 2 s are called long GRBs. This type of GRBs seems to be linked to core-collapse supernovae of massive stars with a mass above 25 solar masses [47].

### Blazars

Blazars are a type of Active Galactic Nucleus (AGN). It is believed that the engine of blazers is the central super massive black hole of a galaxy. The in falling matter forms an accretion disk from which two relativistic jets are emitted back to back. The Doppler boosting in the jet amplifies any flux stemming from the jets [48].
Blazars are known to have a variable flux with flares on time scales of minutes [43] in different energy bands. The observation of the flares in different energy bands is important as it can constrain the emission process but the flares are hard to observe for Imaging Atmospheric Cherenkov Telescopes (IACTs) as the flares are not predictable and the Field of View (FoV) of an IACT is rather small (for H.E.S.S. 5°). Alarms from other experiments with bigger FoV, which can easier monitor Blazers, are used to trigger Target of Opportunity (ToO) observations.
Furthermore blazars allow the study of other physics. As blazars are visible at cosmological distances the Extragalactic Background Light (EBL) can be probed. The EBL consists of the light emitted by galaxies. As gamma rays propagate through the universe they can interact with the EBL creating an

$e^+e^-$ pair modifying the spectrum of blazars at high energies [49].
Constrains on axions models is another topic that can be probed with blazar observations [50]. Axions are candidates for DM, see Chapter 2. They can be probed with blazar observations because photons can, in a magnetic field, convert into axions and vice versa. This oscillation can leave an imprint on the blazars gamma-ray spectrum, for example a high energy photon can convert into an axion close to the blazar and back into a photon close to Earth escaping EBL absorption increasing the expected gamma ray flux at high energies.

#### Supernovae

Massive stars, with masses above 10 solar masses [51], will become supernovae. In the explosion the outer layers will be thrown into inter-stellar space, forming a supernova remnant. Due to the explosion a shock travels through space. When this shock hits the ambient ISM high energy particles are produced. After the acceleration hadronic interaction with the ISM will lead to gamma-rays due to $\pi^0$ decays. Supernovae are considered to be the main source of galactic CR [52].

## 3.2 The Imaging Atmospheric Cherenkov Telescope Technique

The Earth's atmosphere is opaque to photons above energies of around 10 eV. Therefore satellite experiments were the first ones to observe the high energy sky. From tens of MeV up to several hundreds of GeV satellites work well but for VHEs gamma-rays fluxes become too small for satellites to acquire enough statistics in a reasonable time. Furthermore the rather small size of satellites limits their energy and angular resolution for VHEs gamma-rays. Bigger satellites are not feasible cost wise.
At VHE an other technology is needed, IACTs. IACTs use the atmosphere as a calorimeter. Particles entering the atmosphere produce particle showers which can be observed via the Cherenkov radiation produced by the charged particles in the shower. All current IACT experiments are using an array of telescopes consisting of 2–5 telescopes for stereoscopic observations. The stereoscopic observation of showers allows gamma/hadron separation and good event direction reconstruction. For this work the current running H.E.S.S. and the future CTA are used. Details on the data analysis and background reduction are explained in the respective sections. Basic principles of the IACT technique will be described in the following sections.

### 3.2.1 Air Showers

#### Electromagnetic showers

Electromagnetic showers, showers that are induced by photons, electrons or positrons, are very regular because only pair production and bremsstrahlung occurs, two very similar interactions. Therefore a simple model, the Heitler model [53], can be applied to derive the basic properties of an electromagnetic shower. A sketch of the model is shown in Figure 3.1. The Heitler model omits the differences between the interaction lengths and all statistical fluctuations of the interaction length meaning every interaction length $X_0$ photons produce an $e^+e^-$ pair and each lepton produces a photon via Bremsstrahlung. After $n$ interaction lengths there are $2^n$ particles. In the Heitler model the energy is distributed equally over all particles, meaning in the n-th step each particle has $E_n = \frac{E_0}{2^n}$ with $E_0$ being the energy of the primary particle. The shower continues until the energy of the electrons and positrons is below the critical energy $E_c$ where energy loss by Bremsstrahlung is equal to the energy loss by ionization. For air the critical energy is at around 80 MeV. A 1 TeV shower therefore reaches its maximum extension after $n_c = \frac{\log E_0/E_c}{\log 2} \approx 13$ interactions with $N_{max} = \frac{E_c}{E_0} \approx 1 \cdot 10^4$ particles in the shower with an average of 1/3 of them being photons and 2/3 electrons and positrons.

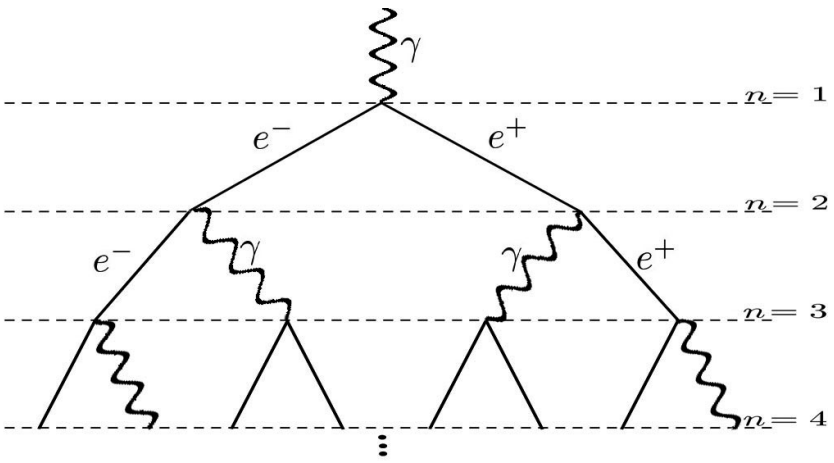


**Figure 3.1:** Sketch of the Heitler model [53]. The incident photon produces an $e^+e^-$ pair. The electron and the positron each produce photons via Bremsstrahlung. The photons produce again $e^+e^-$ pairs. This process continues until the energies go below the critical energy. All interaction length differences and statistical fluctuations are omitted in this model.

**Hadronic Showers**

In contrast to electro-magnetic showers hadronic showers, mostly induced by protons but also heavier nuclei, have a complicated structure. The hadronic interactions will produce many charged particles with different masses giving an irregular emission region for the Cherenkov light. In this hadronic interactions many pions will be produced. The charged pions will decay into myons and neutrino pairs. The neutral pions will produce electromagnetic sub-showers via the $\pi^0 \rightarrow \gamma\gamma$ decay and will therefore lead to a background that must be dealt with. Because the pions are produced in similar amounts one third of the primary particle is deposited in the electromagnetic sub-showers.

### 3.2.2 Cherenkov Radiation

When a charged particle moves in a medium with a velocity higher than the speed of light in that medium the particle can emit coherently light known as Cherenkov radiation [54]. From geometric considerations, see the sketch in Figure 3.2, the opening angle of the cone can be deduced to be

$$\cos\Theta = \frac{\frac{c}{n}t}{\beta ct} = \frac{1}{\beta n}, \tag{3.1}$$

with $\beta$ being the speed of the particle divided by the speed of light in vacuum and $n$ the refractive index of the medium and t the time since the emission of the light. From Equation 3.1 it is clear that for Cherenkov radiation to occur

$$\beta \geq \frac{1}{n}$$

must be satisfied. Considering a 1 TeV particle in 10 km height emitting Cherenkov light, it will illuminate an area with a radius of around 250 m at sea level.
The number of photons $N$ emitted per unit length in a given wavelength interval is given by the Frank-Tamm Formula:

$$\frac{d^2N}{d\lambda dx} = \frac{2\pi\alpha z^2}{\lambda}\left(1 - \frac{1}{\beta^2 n^2}\right) \tag{3.2}$$

with $\alpha$ the fine-structure constant, z the charge of the radiating particle, $\lambda$ the wavelength and $dx$ the length over which the radiation occurs. For a 1 TeV primary photon this leads to approximately 100 photons per $m^2$ in the 300 nm to 600 nm wavelength range at sea level in the light cone produced by the shower [56].

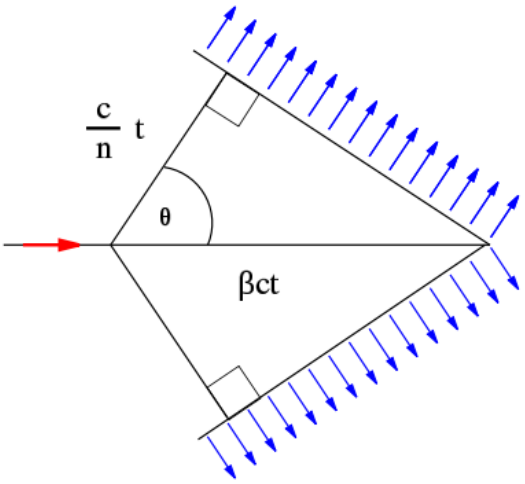


**Figure 3.2:** Sketch of the cone formed by Cherenkov radiation. $\beta$ is the velocity of the particle in units of the vacuum speed of light c. The refractive index of the medium is denoted with n and t is the time since the emission of the Cherenkov light. Taken from [55].

# Chapter 4

# Dark Matter Searches In Dwarf Galaxies With H.E.S.S.

Dwarf Galaxies are as their name suggests small galaxies consisting of up to a few ten billions of stars. In contrast to normal galaxies, dwarf galaxies do not show any signs of star formation. Furthermore no astrophysical gamma-ray source was found in dwarf galaxies up to today. High mass-to-luminosity ratios suggest high concentrations of DM. Furthermore the DM cores of dwarf galaxies are expected to be point-like targets for IACTs and can be analysed with standard analysis methods. Therefore dwarf galaxies are considered promising targets for DM searches.

## 4.1 The H.E.S.S. Array Experiment

H.E.S.S. is an array of initially four telescopes (CT1 - CT4), with a dish diameter of 12 m, placed at the corners of a square with side length of 28 m located in the Khomas Highland in Namibia, Africa. In 2012 a large sized telescope (CT5), with a mirror area of 614 $m^2$, was placed in the center of the array. The array with all five telescopes is also referred to as H.E.S.S. II, see Figure 4.1. Since CT5 only started to take data in 2013 there were no dwarf data with CT5 available when this work was done. Therefore, in the reminder of this work the term H.E.S.S. will only refer to the H.E.S.S. array consisting of CT1-CT4.
The four telescopes allow a stereoscopic reconstruction of air showers observed by at least two telescopes. The stereoscopic observation improves background discrimination, event direction and energy reconstruction.

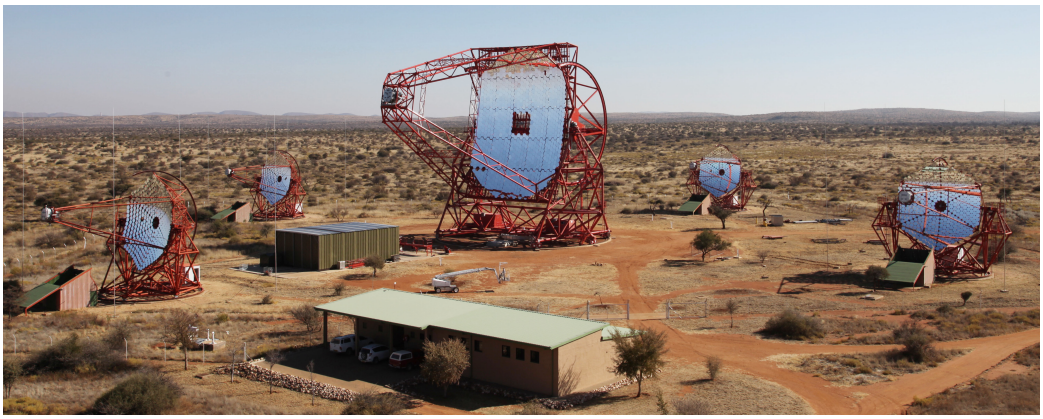

**Figure 4.1:** The H.E.S.S. II array locate in the Khomas Highland in Namibia.

## 4.2 Background Reduction

Gamma-ray sources are relatively faint objects. The brightest, steady and point-like gamma-ray source, the Crab Nebula, has a gamma-ray flux above 1 TeV of around $2 \cdot 10^{-11}\,\mathrm{cm}^{-2}\mathrm{s}^{-1}$ [57] leading to around 6 gamma events per minute for the H.E.S.S. array. Compared to the typical trigger[1] rate of the H.E.S.S. cameras of around 800 Hz [58] it is obvious that a background reduction is important.
Many of these events are from muons and Night Sky Background (NSB) and are only triggering one camera at a time. Therefore H.E.S.S. requires at least two telescopes triggering at the same time. This array trigger lowers the trigger rate of H.E.S.S. down to about 300 Hz. For more details on the H.E.S.S. trigger system refer to [59].
The recorded images still have pixels containing NSB, therefore an image cleaning is used, usually the 0510 image cleaning, meaning only pixels that have an intensity of at least 5 p.e.(photoelectrons) and at least one neighbouring pixel with at least 10 p.e. are used for further parameter determination. The other pixels are set to 0 p.e. so the pixels do not contribute to in further steps of analysis.
After the image cleaning the majority of the recorded events are hadronic events from protons or heavier nuclei. Therefore a gamma-hadron separation must be applied to reduce background contamination further. For the dwarf stacking a MultiVariate Analysis (MVA) [60, 61] is used. MVA is based on Boosted Decision Trees (BDTs). The parameters used to train the BDT are based on Hillas Parameters [62]. For more details on the training parameters refer to [61]. MVA improves the gamma-hadron separation compared to the

[1] At least 3 pixels in one camera have more than 5 p.e.

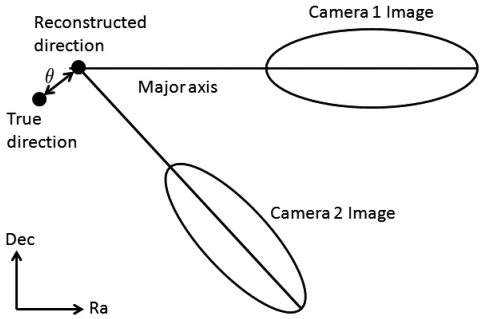


**Figure 4.2:** Sketch of the event direction reconstruction. The intersection of the major axis determines the reconstructed direction. With this method H.E.S.S. reaches an angular resolution $\theta$ of 0.1°.

standard cut based analysis [57] by more then 20% depending on energy and zenith angle [61].
Furthermore the direction of each event is reconstructed. Gamma ray like events produce an elliptically shaped image in the cameras. The intersection point of the major axis of at least two camera images is the reconstructed direction, see Figure 4.2 for a graphic illustration. The angular resolution $\theta$ of H.E.S.S. using this stereoscopic direction reconstruction is about 0.1° in the TeV region.
Even after the gamma-hadron separation there are still hadronic events that are misidentified as gamma-ray events. Therefore the remaining background is estimated from events in the same FoV. In this work the reflected background method is used [57]. In Figure 4.3 a schematic sketch is shown. Typical observations are not pointed directly at the target position ("×") but have an offset observation position ("+"). Assuming that the acceptance in the FoV is only dependent on the radial distance to the observation position background regions (red shaded areas) can be found that have the same angular distance to the observation position as the signal region (blue shaded area) and therefore the same acceptance. By counting the events in the signal and background region the excess events in the signal region can be calculating as

$$n_{excess} = n_{On} - \alpha n_{Off} \tag{4.1}$$

where $n_{On}$ is the number of events in the signal region, $n_{Off}$ the number of events in all background regions summed up and $\alpha$ the normalization factor defined as the number of signal regions (usually 1) divided by the number of background regions.

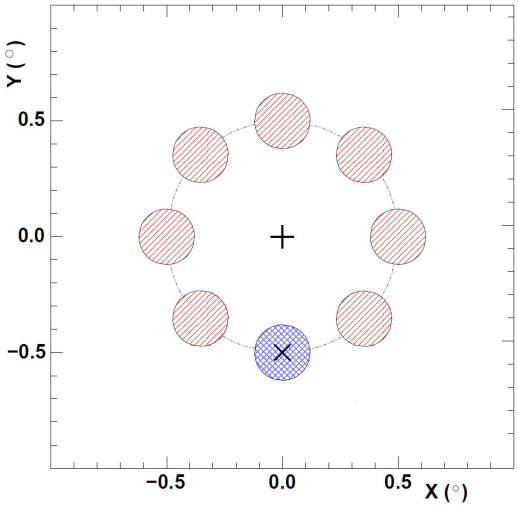


**Figure 4.3:** Schematic view of the reflected background method [57]. The "+" denotes the pointing position of the telescopes. The "×" in the blue shaded region denotes the target position. The blue shaded region marks the signal region, the red shaded regions mark background regions. The background regions have the same offset to the observation position as the signal region to ensure same acceptance in all regions. Original schematic taken from [57].

## 4.3 Dwarf Galaxy Data Set & Analysis

Over the years H.E.S.S. observed several dwarf galaxies. On the most promising ones DM searches were carried out [63–65]. All the limits are still far away from the relic density inferred annihilation cross-section. The limits can be further improved by combining the data sets. In this work 6 dwarfs were used for a stacking analysis. The data sets parameters and standard analysis results ($N_{excess}$, $\sigma$) for the 6 dwarfs is listed in Table 4.1.
The data analysis was done using the HESS Analysis Program (HAP) version hap-12-03-pl01 using Toolkit for MultiVariate Analysis (TMVA) [61] for gamma-hadron separation. TMVA is a special MVA implementation for H.E.S.S.. TMVA uses 6 parameters on which the BDT was trained, Mean Reduced Scaled Width (MRSW), Mean Reduced Scaled Length (MRSL), Mean Reduced Scaled Width Off (MRSWO), Mean Reduced Scaled Length Off (MRSLO), $X_{max}$ and $^{\Delta E}/_{E}$. MRSW was introduced in [57] and is defined as

$$\mathrm{MRSW} = \frac{1}{\sum_{i \in N_{tel}} \omega_i} \sum_{i \in N_{tel}} \left( \frac{W_i - \langle W_i \rangle}{\sigma_i} \omega_i \right). \tag{4.2}$$

$\langle W_i \rangle$ is the mean expected width for a gamma-ray obtained from simulations. $W_i$ is the measured width and $\sigma_i$ the spread of $\langle W_i \rangle$. The weighting $\omega_i$ is

| | $N_{On}$ | $N_{Off}$ | $\alpha$ | $N_{excess}$ | $\bar{\theta}(^\circ)$ | $\bar{z}(^\circ)$ | $T_{obs}$(h) | $\sigma$ |
|---|---|---|---|---|---|---|---|---|
| Sculptor | 177 | 3664 | 0.05 | 3.0 | 0.8 | 14.2 | 12.14 | 0.2 |
| Carina | 268 | 4793 | 0.05 | 7.8 | 0.7 | 33.5 | 22.29 | 0.5 |
| Leo II | 30 | 1962 | 0.02 | −10.0 | 1.7 | 51.0 | 1.73 | −1.7 |
| Fornax | 30 | 1468 | 0.02 | −1.8 | 1.8 | 12.6 | 5.98 | −0.3 |
| Coma-Berenices | 67 | 788 | 0.07 | 12.1 | 0.5 | 47.6 | 3.90 | 1.5 |
| Sagittarius | 1913 | 36497 | 0.05 | 56.7 | 0.7 | 16.0 | 98.61 | 1.3 |

**Table 4.1:** Used dwarf galaxy data set and basic analysis results. Given are number of On events $N_{On}$, off events $N_{Off}$, normalization factor of On and Off region *alpha*, calculated number of excess events $N_{excess}$, the mean offset $\bar{\theta}$ and mean zenith $\bar{z}$ in degree, live time $T_{obs}$ in hours and the calculated significance $\sigma$.

defined as $\omega_i = {\langle W_i \rangle^2}/{\sigma_i^2}$. MRSL is defined in the same way but for the length. MRSWO and MRSLO are the respective mean reduced scale parameters for hadronic events. These two parameters distributions are obtained from simulated background regions also called Off-regions. $X_{max}$ is the shower maximum, the height where the shower reaches its maximum number of particles. ${\Delta E}/{E}$ is the relative average spread of reconstructed energy from all triggered telescopes which still have non zero pixels after image cleaning. The trained BDT delivers one value $\zeta$ for each recorded event. $\zeta$ is a measure for the gamma-ray likeness of the event on which the final gamma-hadron separation cut is performed. The cut values are determined from simulations for different zenith angles and energies. For this work the standard-$\zeta$ cut is used meaning the $\zeta$ cut value is chosen such that the gamma-efficiency is 84% [61].
The observations were done in the wobble observation mode, meaning that the observation position and the target position are offset by an angle between 0.5 and 1.8, see Table 4.1 for the mean offset for each dwarf. This observation mode allows the usage of the reflected background method, described in the last section, for background estimation [41].

## 4.4 J-factors For Dwarf Stacking

The J-factors used in this work were provided by Gregory D. Martinez who used line-of-sight velocity measurements to constrain the dark matter halo profile parameters for the dwarfs using a Bayesian multi-level modelling described in [36]. Because only the line-of-sight velocity can be measured there are ambiguities when the measurements are used to derive a underlying mass profile [66, 67] and therefore the analysis is strongly dependent on the prior

assumptions. The multi-level modelling is used to constrain the prior by first modelling all dwarfs together given their velocity dispersions, half light radii and luminosity. The posterior of the first level is then used as a prior to model the DM distribution for the dwarf galaxies. This method of modelling reduces the uncertainties due to prior assumptions.
The DM density profiles of all the dwarfs were assumed to be following the NFW profile from Equation 2.4. The analysis does not only yield the J-factor but also the uncertainty on the J-factor. Therefore in a profile likelihood analysis the uncertainties can be included to get more robust limits. The results of the analysis for an integration angle of 0.1° is presented in Table 4.2.

| Dwarf | $\log_{10}(J\,[\mathrm{GeV^2cm^{-5}}])$ | $\sigma_{\log(J)}$ |
|---|---|---|
| Sculptor | 18.45 | 0.35 |
| Carina | 18.03 | 0.35 |
| Leo II | 17.51 | 0.21 |
| Fornax | 18.06 | 0.31 |
| Coma-Berenice | 18.82 | 0.35 |
| Sagittarius | 19.11 | 0.54 |

**Table 4.2:** Logaritmic values of the astrophysical factors and the uncertainty $\sigma_{\log(J)}$ for an integration angle of 0.1°.

## 4.5 Dwarf Galaxy Stacking

Stacking data has several advantages. First of all, adding the data will improve the limits as stacked data sets effectively behave like one data set with an overall longer observation time. Furthermore, upwards and downwards fluctuations in single dwarf data sets get smoothed out making the limit more robust.
The stacking analysis follows the profile likelihood presented by W. A. Rolke in [68]. In this work the likelihood consists of three therms

$$L\left(\langle\sigma v\rangle, M_\chi | S, B, \bar{J}\right) = P_s(S,B)P_b(B)P_J(\log(\bar{J}),\sigma) \tag{4.3}$$

with

$$P_s(S,B) = \frac{(S+B)^{n_{On}}}{n_{On}!}e^{-(S+B)} \tag{4.4}$$

$$P_b(B) = \frac{\left(\frac{B}{\alpha}\right)^{n_{Off}}}{n_{Off}!}e^{-\frac{B}{\alpha}} \tag{4.5}$$

$$P_J(\log(J)) = \frac{1}{J\sigma\sqrt{2\pi}\ln(10)} e^{-\frac{(\log(J)-\log(J_0))^2}{2\sigma^2}} \tag{4.6}$$

where $P(S)$ and $P(B)$ are probabilities for observing $n_{On}$ signal and $n_{Off}$ background events given the number of "true" signal events $S$ and "true" background events $B$ for the data set. Both are assumed to be Poisson distributed. $P(\log(\bar{J}), \sigma_{\log(J)})$ is the probabilities that the measured astrophysical $J$ is realized taking into account the uncertainty $\sigma_{\log(J)}$, $\log(J)$ is assumed to be log-normal distributed. Note that "log" denotes the natural logarithm.
The optimal likelihood $L_0$ can be calculated analytically for this case. It turns out the likelihood is maximal for

$$S = n_{On} - \alpha n_{Off} \tag{4.7}$$
$$B = \alpha n_{Off} \tag{4.8}$$
$$\log(J) = \log(J_0). \tag{4.9}$$

The velocity averaged annihilation cross section $\langle\sigma v\rangle$ is connected to the true signal $S$ by

$$S = \frac{1}{8\pi m_\chi^2} \langle\sigma v\rangle J \int_E \int_{\Delta\Omega} A_{eff}(E,z) \frac{dN}{dN_\gamma} d\Omega dE. \tag{4.10}$$

The likelihood is maximized given the events counts from the observations, for details see Appendix A for details on the optimizations procedure.
The next step is to calculate the profile Likelihood

$$\lambda = \frac{L\left(\langle\sigma v\rangle, M_\chi | S, B, \bar{J}\right)}{L_0} \tag{4.11}$$

there $L_0$ is the maximized likelihood while $L$ is the maximized likelihood for fixed $\langle\sigma v\rangle$. According to the Wilks' theorem $-2\log(\lambda)$ is $\chi^2$ distributed [69], therefore to calculate the 95% upper limit the $\langle\sigma v\rangle$ value for which

$$2\log\left(\lambda_{95\%}\right) - 2\log\left(\lambda_0\right) = 2.71 \tag{4.12}$$

holds true must be computed. For the stacked data set, $\log\lambda$ in Equation 4.12 consists of the sum of all $\log\lambda$ of all dwarfs.
For weak signals this method can yield negative true signals counts $S$, which also means a negative annihilation cross section, and therefore a non physical result. To avoid that problem in [68] two methods are suggested. The first method suggests adding events in the signal region until the estimator for $S$ is than 0. That method works without a problem if there is only one signal

region but each dwarf galaxy is a signal region in it self, so for the stacked data set there is no one signal region.
The second method suggested is to use $\lambda$ at $\langle \sigma v \rangle = 0$ instead of the best estimator. The resulting limit will result in a slight over coverage but is easy to implement therefore the second method was used for negative estimators.

## 4.6 Stacking Results

The limits are calculated for the Bergstrom annihilation spectrum [70] given by

$$\frac{dN_\gamma}{dE} = \frac{0.73}{x^{1.5}} e^{-7.8x} \tag{4.13}$$

with $x$ being the energy divided by the assumed WIMP mass $x = \frac{E}{m_\chi}$. This spectrum includes the contribution from DM annihilating into $WW$, $ZZ$. The annihilation spectrum was used for $0 \leq x \leq 1$. For $x > 1$ the annihilation spectrum was set to be zero, because thermal DM will only only produce gamma rays up to the DM mass.
In Figure 4.4 the limits for every single dwarf galaxy as well as the combined result are shown. On the left hand side of Figure 4.4 the combined limit includes the Sagittarius dwarf. It is obvious, that the Sagittarius dwarf dominates the combined limit because the Sagittarius dwarf limit is about two orders of magnitude lower than the other limits. This is due to the longer observation time and the higher astrophysical factor.
On the right hand side the combined limit is shown for all the dwarfs except for the Sagittarius dwarf because the Sagittarius dwarf is tidally disrupted by the Milky Way [71]. Therefore it is debated if the assumptions for the J-factor calculations hold true for the core region or if the modelling fails for Sagittarius.

Compared to the Fermi LAT dwarf stacking results [72], see Figure 4.5 and Table 4.3 for the used J factors and their uncertainties, the improvement from single limits to the combined limit is small for the case without Sagittarius and negligible then Sagittarius is included while the Fermi result show a clear improvement compared to the single results. This is due to Fermi having a far more uniform observation of the single dwarfs because Fermi LAT covers the whole sky in 3 h [73] and has a FoV of 2.4 sr ($\approx 103°$) [74]. Therefore Fermi LAT has more dwarfs, see Table 4.3, and the limits of comparable dwarfs with similar J-factors are similar.

Furthermore as shown in [75] the uncertainties on the astrophysical factor are minimal for a special integration angle $\alpha_c$. This optimal integration

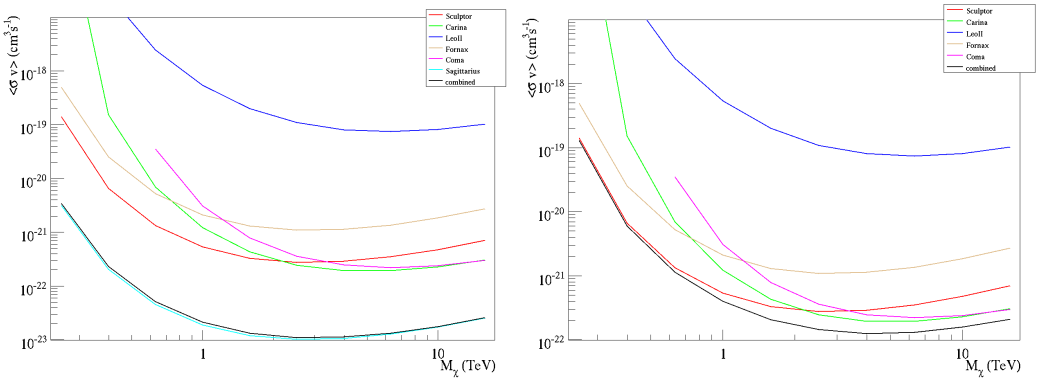


**Figure 4.4:** 95% CL upper limits from the dwarf stacking for the astrophysical factors and their uncertainties from Table 4.2. On the left hand side the results for all six dwarfs are shown. On the right hand side for five dwarfs, excluding the Sagittarius dwarf galaxy, are shown. The combined limit is dominated by the Sagittarius dwarf due to the lager livetime and the high astrophysical factor.

| Dwarf | $\log_{10}(J\,[\mathrm{GeV}^2\mathrm{cm}^{-5}])$ | $\sigma_{\log_{10}(J)}$ |
|---|---|---|
| Bootes I | 17.7 | 0.34 |
| Carina | 18.0 | 0.13 |
| Coma Berenices | 19.0 | 0.37 |
| Draco | 18.8 | 0.13 |
| Fornax | 17.7 | 0.23 |
| Sculptor | 18.4 | 0.13 |
| Segue 1 | 19.6 | 0.53 |
| Sextans | 17.8 | 0.23 |
| Ursa Major II | 19.6 | 0.40 |
| Ursa Minor | 18.5 | 0.18 |

**Table 4.3:** Astrophysical factors and their uncertainties used in the Fermi LAT dwarf stacking analysis, extracted from [72]. Note that the uncertainties are mostly lower than the values for H.E.S.S. because the angular resolution of Fermi LAT is closer to the optimal integration region.

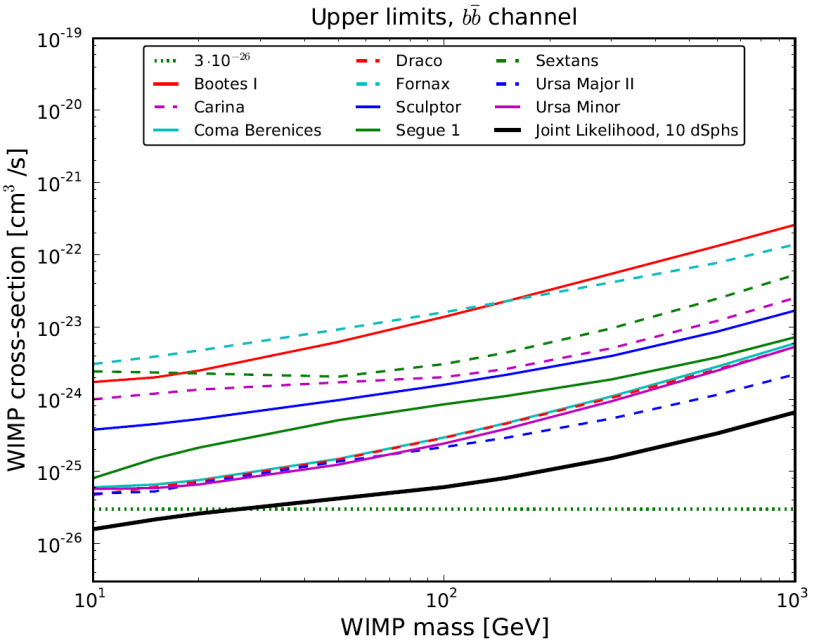


**Figure 4.5:** Fermi LAT 95% CL limits of the dwarf stacking for 10 dwarfs with a $b\bar{b}$ annihilation spectrum. The uniform observation of Fermi gives similar limits for the single dwarfs. The stacking improves the limit. Plot from [72].

angle, the angle there the uncertainties on $\log_{10}(J)$ become minimal, is dependent on the dwarf but usually is around 0.3° to 0.4°, see Figure 4.6, and is therefore closer to Fermi LAT angular resolution, which varies between 0.2° and 1° in the energy range 1 GeV − 100 GeV [76], then to the angular resolution of H.E.S.S. of ≈ 0.1°. Even if the optimal integration angle is smaller then Fermi LAT angular resolution the uncertainties on $J$ are normally still smaller for integration angles $> \alpha_c$ then for 0.1°.

Though Fermi LAT seems to outperform H.E.S.S. it is important to note that Fermi LAT can not constrain DM annihilation at energies above a few TeV because the energy resolution and the effective areas of Fermi LAT become worse so that H.E.S.S. becomes important. The derived H.E.S.S. dwarf stacking limits are three orders above the annihilation cross-section inferred from CMB observations, see chapter 2 for the case including Sagittarius and four orders if Sagittarius is excluded.

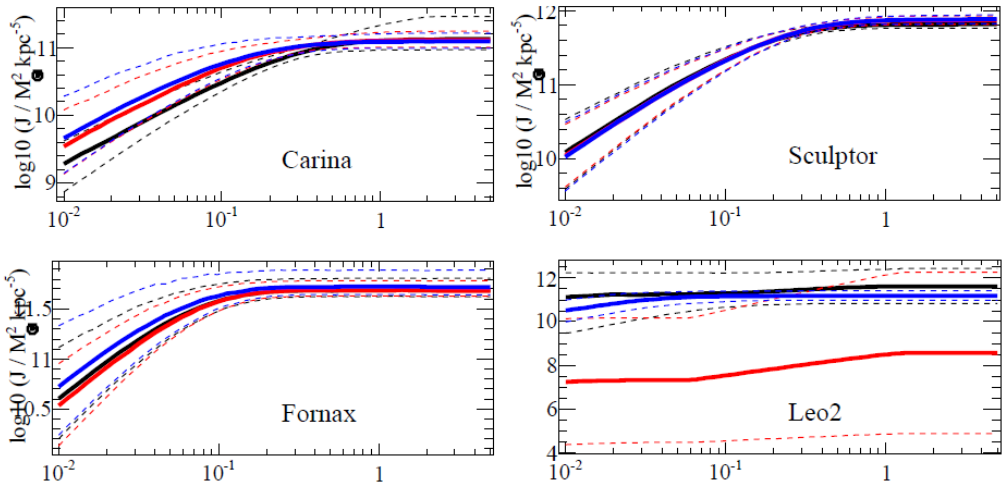


**Figure 4.6:** Astrophysical factor as a function of the integration angle $\alpha$ for the four dwarfs that were used in this work and also analysed in [75]. The modelling uncertainties are minimal for integration angles of $> 0.1°$ usally well in Fermi LATs angular resolution of $0.2° - 1°$ [76]. Plots extracted from [75].

# Chapter 5

# A Dark Matter Search In The Galactic Center Region With The Future Cherenkov Telescope Array

The best DM limits from H.E.S.S. is from the Galactic Center (GC) region [77]. As can be seen in Figure 5.1. The limits were calculated for a 112 h data set. It turns out that the limit is still one order of magnitude above $3 \cdot 10^{-26}\,\mathrm{cm^3 s^{-1}}$. Considering the limit should improve with the square root of the observation time meaning to lower the limit by an order of magnitude a 100 times longer observation campaign would be needed. IACTs have typical 1000 h of observation time per year. It is obvious that current IACTs reached their limit. A new system is needed. This system will be CTA. CTA will have improved sensitivity compared to the current generation of Cherenkov telescopes by at least an order of magnitude. The improved sensitivity will expand the physics CTA can study compared to current generation IACTs. Also DM searches will be carried out on many sources like dwarf galaxies, galaxy cluster and others [78]. In this chapter the prospects for DM halo searches with different observation strategies are presented. This chapter will present the prospect for DM searches for CTA in the GC region.

## 5.1 The Cherenkov Telescope Array

The CTA will be the successor of current IACTs and the first open observatory for ground based gamma-ray observations. CTA will improve in

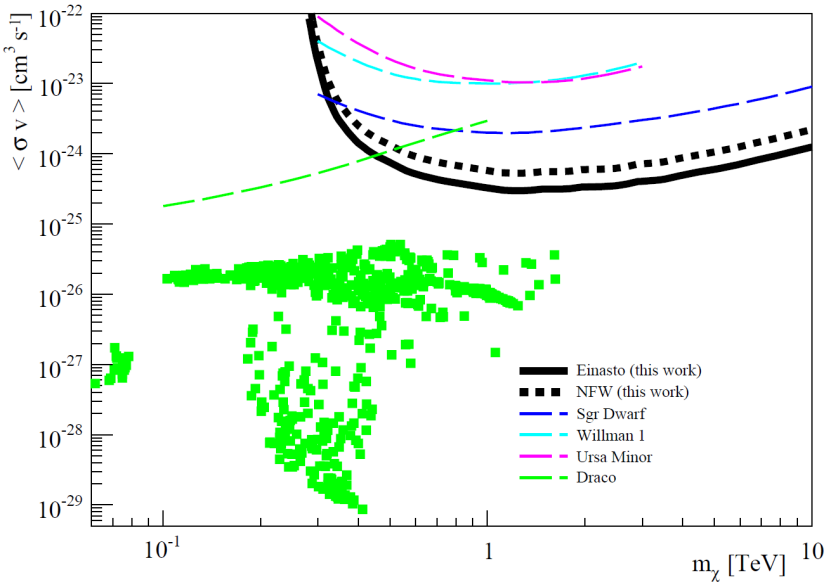


**Figure 5.1:** H.E.S.S. limits for the GC region. The GC was observed for 112 h. The limits are one order of magnitude abouve the expected annihilation cross-section of $3 \cdot 10^{-26}\,\mathrm{cm^3 s^{-1}}$. The Plot was extracted from [77]. The green squares represent mSUGRA models that are in agreement with WMAP and collider data.

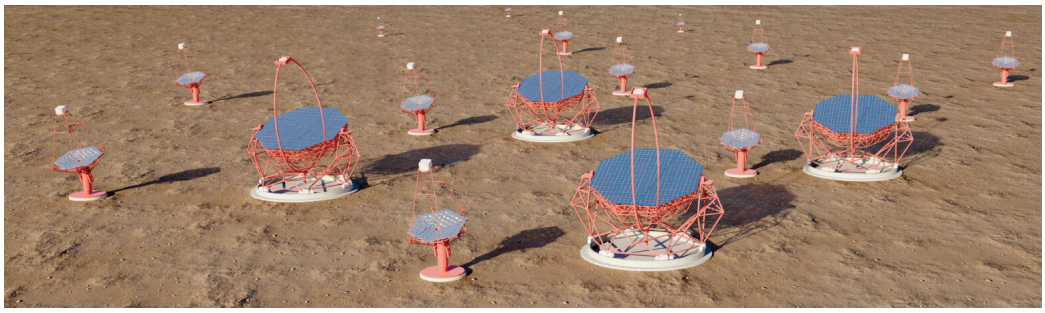

**Figure 5.2:** Artist impression of a possible CTA array.

sensitivity by about an order of magnitude compared to the current generation of IACTs. Figure 5.2 shows an artist impression of the CTA array. The energy range will extend from well below 100 GeV to above 100 TeV. To accomplish these goals CTA will consist of 50-80 telescopes composed of three different telescope types with different dish sizes.

Different arrays, with different numbers of each telescope type and telescope layout, are under investigation by the CTA Consortium using Monte Carlo (MC) simulations. For a detailed description of the MC methods and the array performances see [79]

## 5.2 The Galactic Center Region

The GC region is an interesting target for DM searches. High resolution N-body simulations like the Aquarius Simulation [80] and Via Lactea II [81] predict high DM densities at the GC.
But as can be seen in Figure 5.3 the GC also contains strong astrophysical sources like the GC source [82], probably related to either the central Black Hole Sgr A* or the pulsar wind nebula G 359.95-0.04 [83], and diffuse emission extending 0.3° above and below the galactic plane, originating from hadronic interactions of cosmic rays with molecular clouds [84].
The GC source itself does not pose a problem. It is a well known source contained in a small region with an angular extension of 0.1°; events originating from that region can be excluded from the analysis. The diffuse emission on the contrary has a quite complicated structure, see Figure 5.3. Moreover the diffuse emission gets weaker with increasing distance to the galactic plane meaning it can mimic the DM signal. To avoid diffuse emission contamination, parts of observations with galactic latitude $|b| < 0.3°$ are excluded from the analysis.

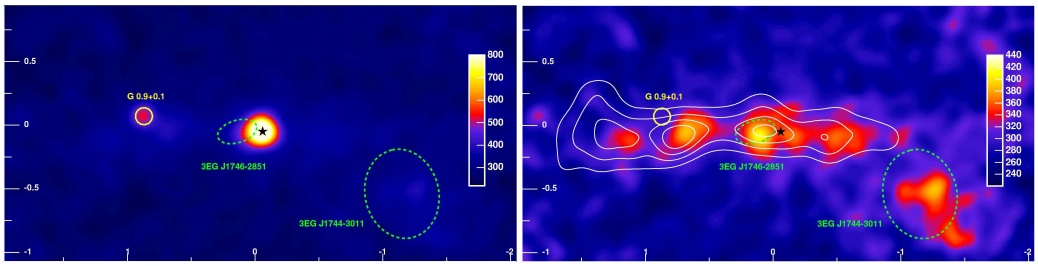


**Figure 5.3:** The GC region as seen by H.E.S.S.. On the left hand side the gamma-ray sources SNR G0.9+0.1 (yellow circle) and SgrA* (star shaped marker) are shown. On the right hand side the strong gamma-ray sources were subtracted to make faint gamma emissions, like the emission along the galactic plane, visible. Because the diffuse emission can not be distinguished, by event counts only, from the DM signal the region with galactic latitude $|b| < 0.3°$ is excluded from all analyses. Both pictures were extracted from [84].

## 5.3 CTA Candidate Arrays

The final array layout for CTA is not decided yet and several MC studies are carried out to study the impact of different layouts on possible physics results. At the time this thesis was written MCs were in the production 1 stage and only for two arrays off-axis performances were available. The arrays are simply called Array B and Array E. Array E is an all purpose array consisting of a total of 58 telescopes with 4 Large Size Telescopes (LSTs), 23 MSTs and 31 Small Size Telescopes (SSTs). Array B is optimized for lower energies with 42 telescopes, only using two sizes of telescopes, 5 LSTs and 37 MSTs, and a more compact design, see Figure 5.4. Table 5.1 lists the number of different telescope types and their FoV for the arrays. The effective areas and background rates used in this section were derived from the IFEA MC analysis. The IFEA analysis is working with a Hillas parametrization [85] for event reconstruction with added parameters. The added parameters and constrains are the fraction of light in the two brightest pixels in the ellipsoid, a minimum of 50 p.e. in the image amplitude and the image centroid must be within the inner 80% of the FoV. A Random Forest (RF) for background suppression as used by Major Atmospheric Imaging Cherenkov Telescope (MAGIC) [86] is also used in the MC. One RF consisting of 100 trees is used for each telescope type. The RF delivers a single number between 0 and 1 the hadronness for each image. Depending on the reconstructed energy and offset to the camera center a cut is applied on the hadronness. The simulations assume that CTA is at 2000 m altitude and the observations are performed at 20° zenith with an array placed in the southern hemisphere. The hemisphere is important

| Array | # LST | FoV | # MST | FoV | # SST | FoV |
|---|---|---|---|---|---|---|
| E | 4 | 4.6° | 23 | 8° | 31 | 10° |
| B | 5 | 5° | 37 | 8° | 0 | – |

**Table 5.1:** Number of telescopes of different size and the FoV of each type for possible array configurations used in this thesis. For telescope arrangement see Figure 5.4.

because the charged particles in the shower are deflected by the magnetic field altering the shower image in the camera and because the GC is visible at low zenith angle from the southern hemisphere. For a detailed explanation of the analysis see [87].
In Figure 5.5 the used effective areas are shown. The FoV increases for higher energy as different sized telescopes become important. To compare Array B and E a slice through the first off-axis bin is shown in Figure 5.6. From 25 GeV up to around 1.6 TeV Array B has higher effective areas as Array E due to its more compact layout and the five LSTs.
In Figure 5.7 the rate of remaining background events per second per square degree is shown. These background events can not be further reduced by the RF analysis and must be taken into account in the later analysis. Similar as for the effective areas the FoV increases for higher energies. Also at high energies the arrays are nearly background free.
In the following sections of this work the standard assumption that the acceptance of the observation is radial symmetric is used.

## 5.4 Ring Method

In this section, the Ring Method, a method using the same FoV for signal and background estimation, will be presented. The advantage of the Ring Method compared to the On-Off method presented in Section 5.5 is clear, all observations are carried out in a region were high DM annihilation fluxes are expected, no time is "wasted" to take data in control regions. The disadvantage on the other hand is that also rather high DM annihilation fluxes are expected in the background estimation region, therefore lowering the sensitivity.

### 5.4.1 Optimizing the Ring Method

A Milky Way halo DM search was carried out by H.E.S.S. [89]. The limit derived in that analysis is the best DM annihilation limit from IACT, see

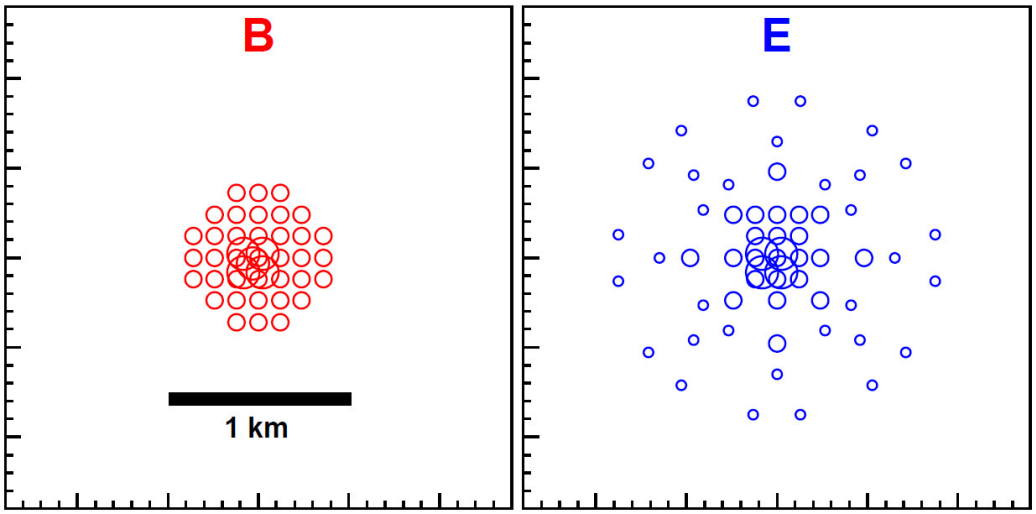


**Figure 5.4:** Possible CTA array configurations used for this thesis. Circle size corresponds to telescope size. Array B is optimized for lower energies and has therefore a more compact design and no SSTs. Array E is an all purpose array and uses all sizes of telescopes. Picture extracted from [88].

Figure 5.1. In that work the background regions were constructed by searching for pixels that have the same angular distance to the pointing direction as pixels in the signal region. The analysis has the limitation that the search for background pixels only considers pixel that are rotated by 90°, 180° or 270° with respect to the signal region. In this work this restriction is removed.
The Ring Method, see Figure 5.8 for an illustration of the parameters, is using a ring around the observation position with inner radius $r_1$ and outer radius $r_2$ leading to regions with equal acceptance. The Ring Method chooses the signal region as the part of the ring that has an angular distance to the GC smaller than $\Delta_{\text{cut}}$; the rest of the ring is used as background region. This construction guarantees the signal region is closer to the GC and therefore has a higher DM annihilation flux than areas in the background region. Furthermore the galactic plane (galactic height $|b| \leq 0.3°$) is excluded from signal and background regions (yellow area in Figure 5.8)
For each array the parameters $\Delta_{cut}$, $r_1$, $r_2$ and the galactic height of the observation position $b$ were varied to find the best values to reach a $5\sigma$, as defined by Li & Ma [90], DM detection as fast as possible assuming the Tasitsiomi annihilation profile [91]

$$\frac{dN}{dx} = \frac{10}{3} + \frac{5}{12}x^{-1.5} - \frac{5}{4}\sqrt{x} - \frac{2.5}{\sqrt{x}}, \tag{5.1}$$

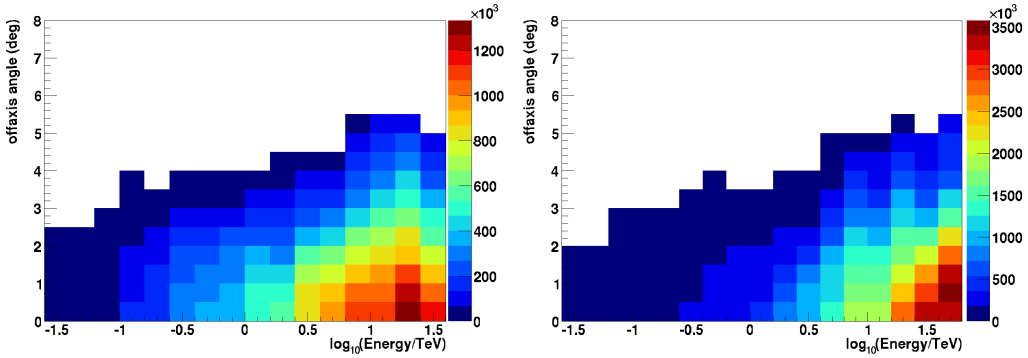


**Figure 5.5:** Off-axis performance of Array B (left) and Array E (right). The color code represents the effective area in $m^2$. Clearly visible is how the FoV grows with higher energies. For a projection of the first off-axis bin to compare Array B with Array E see Figure 5.6.

| Array | $b$ | $r_1$ | $r_2$ | $\Delta_{cut}$ |
|---|---|---|---|---|
| E | 1.42° | 0.55° | 2.88° | 1.36° |
| B | 1.40° | 0.44° | 2.50° | 1.29° |

**Table 5.2:** Optimized parameters for the Ring Method using Tasitsiomi profile [91] and astrophysical factor from the Aquarius simulation [80]. See Figure 5.8 for a description of the parameters.

with $x = \frac{E}{m_\chi}$ and the DM halo profile from the Aquarius simulation [80] to calculate the signal rate in the signal and background region while the background rates were estimated using the results of the MC shown in Figure 5.7. The results show a mild dependence on the DM mass because the FoV of CTA depends on energy but because the dependence turned out to be small so that the values averaged over the DM masses were used, see Table 5.2 for optimized values. Also see Table 5.3 for the resulting average integrated astrophysical factors in the resulting signal regions.

### 5.4.2 Limit Extraction

In contrast to dwarf galaxies where the expected annihilation region is contained in a small part of the FoV ($\mathcal{O}(0.1°)$) the annihilation region in halo searches extends over the whole FoV. Therefore the background estimation region is expected to contain events from DM annihilation that have has to be taken into account when calculating the limits. The rate of excess photon events $R_s - \alpha R_b$, with $R_s$ being the rate of events in the signal region and

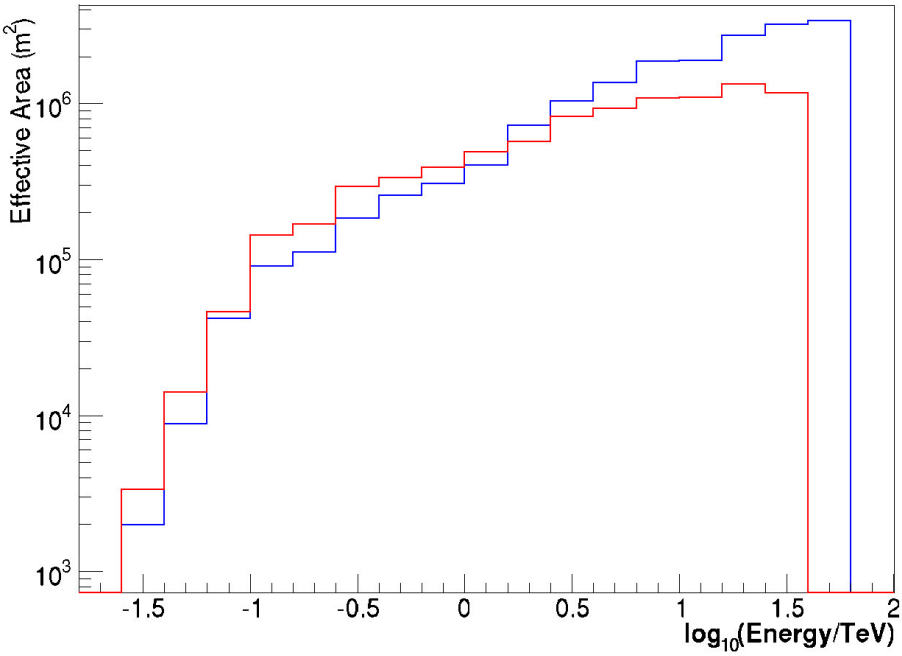


**Figure 5.6:** Effective areas of Array B (red) and Array E (blue) as a function of the energy. Due to the more compact layout and the five LSTs the effective areas of Array B are higher then Array E's up to an energy of $\approx 1.6\,\mathrm{TeV}$. For higher energies Array E takes over.

$R_b$ the rate of events in the background region, is therefore defined as

$$\frac{\langle\sigma_{ann}v\rangle}{8\pi m_\chi^2}\int_{E_{thr}}^{m_\chi} dE\frac{dN_\gamma}{dE_\gamma}\left[\int_{\Delta\Omega_s} J(\varphi)A(\Omega,E)d\Omega - \alpha\int_{\Delta\Omega_b} J(\varphi)A(\Omega,E)d\Omega\right] \tag{5.2}$$

with $\alpha = \Delta\Omega_s/\Delta\Omega_b$ the relative size of signal and background region and $\varphi$ the angular distance to the GC. With a given observation time, usually 100 h[1], and using the Feldmann-Cousin method from [92] the 95% CL upper limit on the number of excess events can be calculated and translated to a 95% CL limit on $\langle\sigma v\rangle$. To calculate the average upper limit instead of putting the number of signal and background events calculated with the rates directly into the Feldmann-Cousin algorithm, random Poisson distributed events with expected value equal to the background and signal event counts were used. 1000 limits for each DM mass were calculated and averaged in the end.
The results for several annihilation spectra taken from [27, 28] and an obser-

[1] 100 h are approximately 10% of the observation time available over a whole year and can reasonably be acquired for a source in one year.

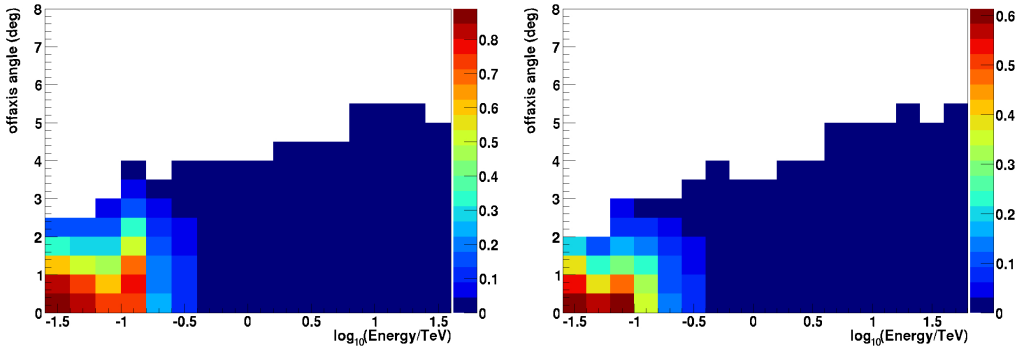


**Figure 5.7:** Background rates of Array B (left) and Array E (right). The color codes represents the background event rates in Hz per square degree.

| Method | Array | $\widetilde{J}_s$ ($10^{22}\,\mathrm{GeV^2cm^{-5}}$) | $\Delta\Omega_s$ (sr) |
|---|---|---|---|
| Ring | E | 4.68 | 0.00117 |
| | B | 4.43 | 0.00104 |

**Table 5.3:** Average $\widetilde{J}_s$ values for Array E and B, using the Ring method, and solid angle $\Delta\Omega_s$ of the signal region.

vation time of 100 h can be seen in Figure 5.10. All annihilation channels are reaching close to or even reach below the expected annihilation cross-section of $\langle\sigma v\rangle = 3 \cdot 10^{-26}\mathrm{cm^{-3}s^{-1}}$. Especially WIMPs that annihilate mainly into $\tau^+\tau^-$ can be interesting because in a energy range from below 0.1 TeV to $\approx 2$ TeV the limit for $\tau^+\tau^-$ crosses the $\langle\sigma v\rangle = 3 \cdot 10^{-26}\mathrm{cm^{-3}s^{-1}}$ line, meaning models predicting WIMPs mainly annihilation into $\tau$ leptons can be easily detected or excluded. Additionally, the limits for both arrays are quite similar with Array B being slightly better then Array E showing the importance of low energy performance of the array even for high mass WIMPs because most of the photons that are produced in the annihilation have low energies.

## 5.5 On-Off Method

The On-Off Method is a method where the background is estimated using a dedicated background observation, that is called Off observation (in contrast to the signal region observation that is called On observation). In other words typically half of the observation is taken with the telescopes pointing at a signal free position. The advantage is that the background FoV does not contain high DM annihilation fluxes giving a cleaner estimate of the background than the Ring method.

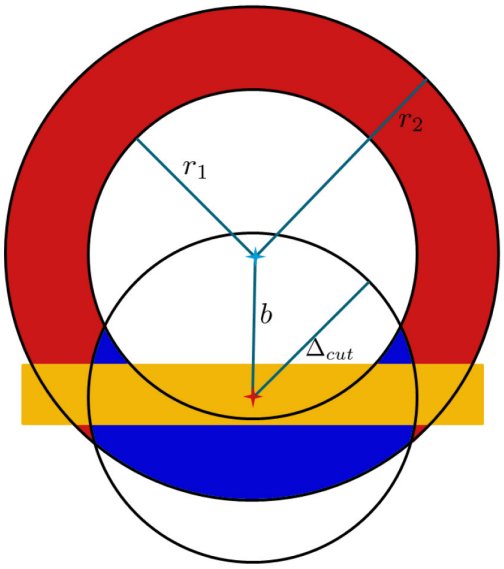


**Figure 5.8:** Sketch of the Ring Method showing the construction of signal and background regions in the FoV. The red star denotes the GC position. The blue star shows the observation position, which is displaced to the GC by $b$ in latitude. The annulus with inner and outer radii $r_1$ and $r_2$ around the observation position defines regions of equal acceptance. The intersection of the annulus with a circle around the GC with radius $\Delta_{cut}$ defines the signal region (blue area). The remaining area of the annulus (red) is the background region for the analysis. To avoid contamination from diffuse emission along the galactic plane regions with galactic latitude of $\pm 0.3°$ (yellow) were excluded from signal and background region.

It is important for the Off observation, that the zenith and azimuth distribution is the same as in the On observation to ensure same acceptance and that the data taking conditions in both observations are identical. Same observation conditions and zenith and azimuth coverage is guaranteed by

a) taking On and Off runs consecutively to minimize changes in atmospheric conditions and

b) pointing the telescopes to the same zenith and azimuth coordinates at the beginning of the observations so that the tracking can follow the same path in zenith and azimuth.

But even if zenith and azimuth distributions are the same and the atmospheric conditions does not change, the Off observations can have significantly different data rates due to differences in the NSB and number of stars in the FoV. This thesis assumes that all the systematics of NSB and stars

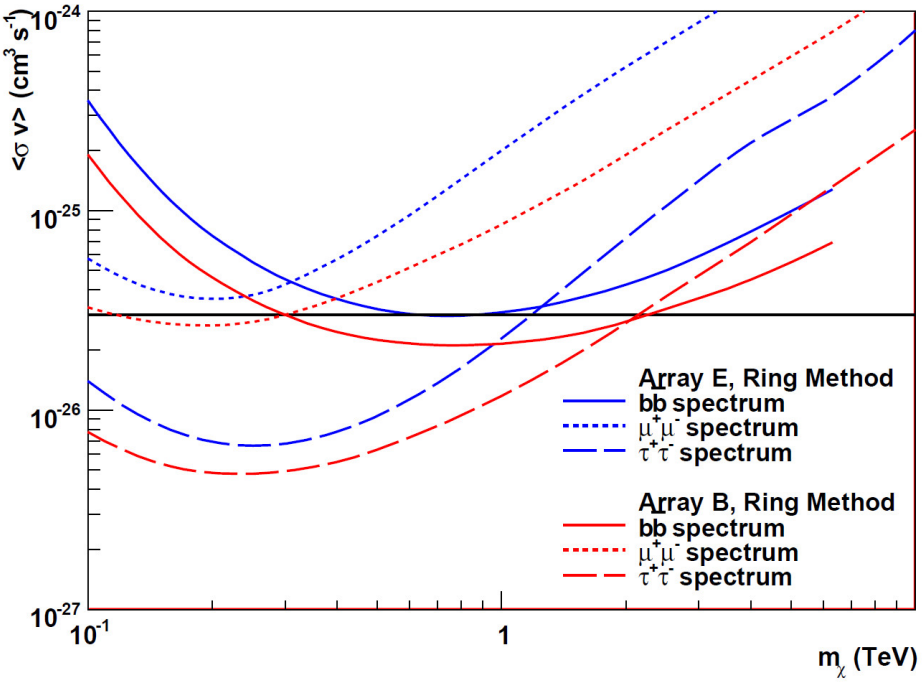


**Figure 5.9:** 95% CL upper limits for Array B and E using three different annihilation spectra and an observation time of 100 h. $\tau^+\tau^-$ is especially promising.

in the FoV are well understood and under control by the time CTA is operational.
On-Off observations have the advantage that the difference of the astrophysical factor of the FoVs is higher than in the Ring-Method possibly leading to higher sensitivity.
As in the Ring Method the areas with galactic latitude of $\pm 0.3°$ is excluded from the signal region. To ensure exactly same acceptances in the background region the corresponding areas in the background region are also excluded. An interesting feature of the On-Off method used with CTA is that the effective FoV increases with the DM mass because the different telescope types have different energy thresholds and different FoVs. The increased FoV yields higher astrophysical factors for higher DM masses, see Table 5.4. As expected the astrophysical factor is higher than for the Ring method.
The limit calculation proceeds analogue to the limit calculation for the Ring Method except that the observation time is assumed to be evenly divided between On and Off observations. The results can be seen in Figure 5.10 where the limit from 50 h + 50 h On-Off data is compared to limits for the Ring Method with 100 h of data. Both methods are using the Tasitsiomi annihilation profile. As expected the On-Off Method performs better over

| Method | Array | $m_\chi$ (TeV) | $\widetilde{J}_s$ ($10^{22}\,\mathrm{GeV^2cm^{-5}}$) | $\Delta\Omega_s$ (sr) |
|---|---|---|---|---|
| On-Off | E | 0.1 | 16.4 | 0.00751 |
| | | 1 | 19.7 | 0.01044 |
| | | 10 | 28.7 | 0.02211 |
| On-Off | B | 0.1 | 16.4 | 0.00751 |
| | | 1 | 22.8 | 0.01384 |
| | | 10 | 28.7 | 0.02211 |

**Table 5.4:** Average $\widetilde{J}$ factors for Array E and B using On-Off. Because telescopes have different energy thresholds the FoV changes and therefore also $\widetilde{J}_s$ and the solid angle $\Delta\Omega_s$.

the whole mass range. Both arrays reach $\langle\sigma v\rangle = 3\cdot10^{-26}\mathrm{cm^{-3}s^{-1}}$ with Array B again giving better results due to the lower energy threshold.

## 5.6 Summary

As shown in this section CTA has the potential to reach the annihilation cross-section expected from the relic density calculations with halo searches regardless of the method used. This is a great improvement compared to current IACTs. CTA could be the first Cherenkov telescope able to probe different DM models. Even though the annihilation spectra used in this work are all conservative spectra in the sense that the spectra do not have any enhancements like internal Bremsstrahlung [93] or the Sommerfeld enhancement [94] which would improve the limits even further.
Even though the On-Off method yields better limits, the Ring Method will probably be used in the future. The improvement of the On-Off method is not big enough to justify to "waste" valuable observation time on an empty FoV, if similar results can be reached with the Ring method while also analysing interesting standard sources such as the GC source or diffuse emission. That argument could be weakened by the observation offset used for the Ring method. In H.E.S.S. the standard observation offset is $\approx 0.5°$. Compared to that the 1.4° offset is considerably higher. But the standard offset for CTA for point-like sources is not clear yet. The performance of the Ring method will be affected by the standard observation offset. Furthermore if an interesting gamma-ray source is found in a suitable Off region, for example by an extra-galactic scan done by CTA, the situation could change in favour for the On-Off method.

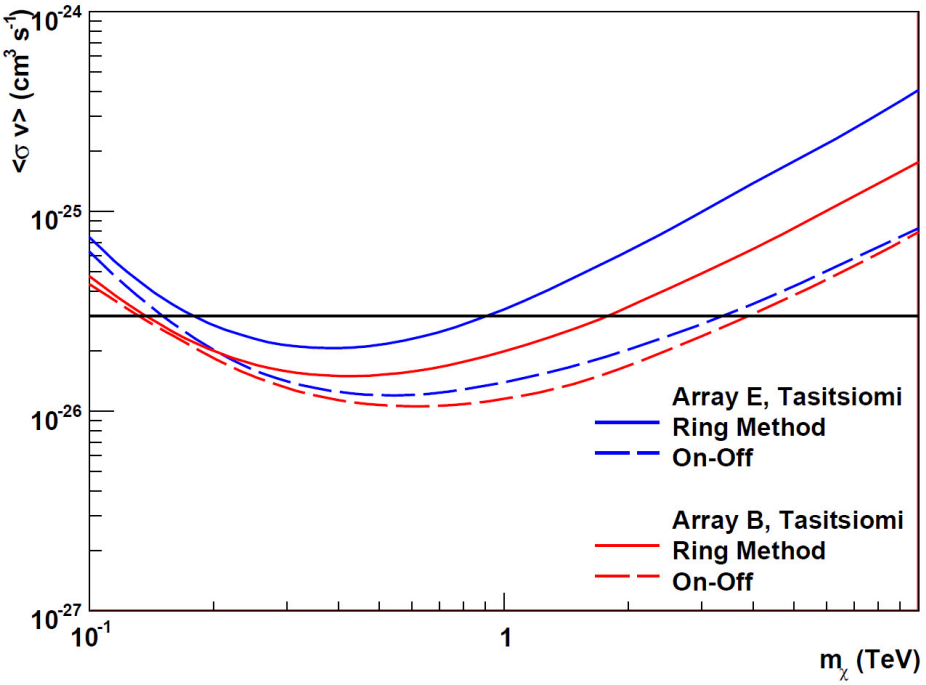


**Figure 5.10:** Comparison of the Ring Method with the On-Off Method. The limits are calculated for 100 h of data for the Ring Method and 50 h + 50 h for the On-Off method. The On-Off Method outperforms the Ring Method over the whole mass range.

# Chapter 6

# Summary & Conclusions

Many experiments are dedicated to detect DM via direct and indirect methods. The indirect methods are looking for particles produced by DM annihilation or decay. Photons are one type of messenger particle. In contrast to charged messenger particles photons are not deflected by the galactic magnetic fields, which allows the direct observation regions where the DM concentration is expected to be high.
Figure 6.1 shows various current limits and the limits derived in this thesis. As shown in this work, with current generation IACT systems it will be hard to reach the velocity averaged annihilation cross-section implied by CMB observations making a detection of DM annihilation not probable. Limits derived from dwarf galaxy observations by H.E.S.S. are two orders of magnitude above the relic annihilation cross section (Section 4). The limits from GC observations with H.E.S.S. [77] are one order of magnitude better because the expected DM density is higher but still the limits are too high to yield results that could exclude interesting DM candidates.
Much longer observations to improve the limits significantly are not feasible as the limit scales only with the square root of the observation time. Therefore the future CTA is needed for DM searches with Cherenkov telescope experiments. As shown in Section 5 the limits for CTA GC halo searches will reach the relic annihilation cross-section in a WIMP mass range from $\approx 100\,\mathrm{GeV}$ up to several TeV. As seen in Figure 6.1 the CTA GC limit will be better than the Fermi dwarf galaxy stacking for DM masses above a few 100 GeV. Even considering that Fermi will continue to accumulate more data from dwarf observations (green dashed line in Figure 6.1) CTA will still outperform Fermi at energies above 200 GeV. Together CTA and Fermi will be able to probe WIMP candidates from $\approx 10\,\mathrm{GeV}$ up to a few TeV.

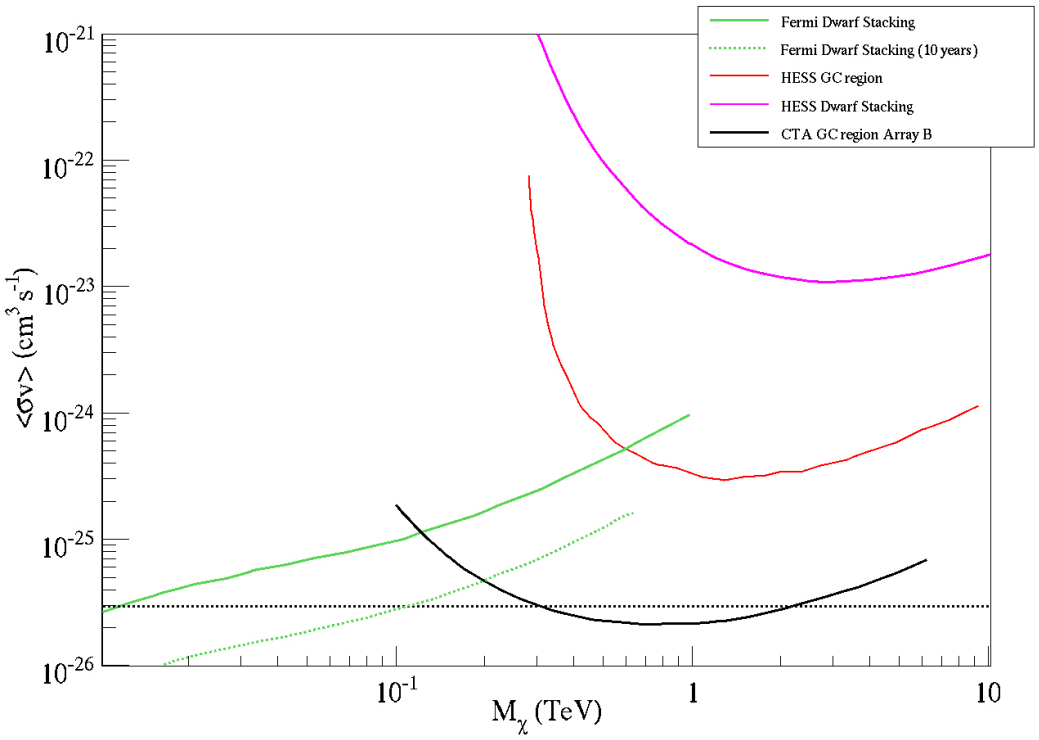


**Figure 6.1:** Comparision of DM velocity averaged annihilation cross-section limits from gamma-ray observations. The dotted black line is the velocity averaged annihilation crossection infered from the relic density. The green solid line represents the dwarf stacking results of Fermi [72] and the dashed green line a scaled limit for a possible 10 year result for dwarf stacking with Fermi and annihilation into $b\bar{b}$, extracted from [95]. Below 500 GeV this limit is the best to date. Above 500 GeV the H.E.S.S. GC region (red) limits takes over [77]. In puple and black are the results of this thesis. Purple is the limit for the dwarf stacking with H.E.S.S. (for all six dwarfs). The limit is more than one order of magnitude abouve the H.E.S.S. GC limits. The solid black line is the limit for CTA GC using the Ring Method for array B and annihilation into $b\bar{b}$. The improvement in sensitivity of CTA compared to current IACTs will allow to reach below $\langle\sigma v\rangle = 3 \cdot 10^{-26} cm^3 s^{-1}$ for DM masses from around 0.3 TeV to 2 TeV.

# Appendix A

# Optimization Of The Estimators Of Background And Astrophysical Factor

The log-likelihood for the dwarf stacking consists of three components:

$$\mathcal{P}_s = n_{On} \ln(S+B) - (S+B) \tag{A.1}$$

$$\mathcal{P}_b = n_{Off} \ln\left(\frac{B}{\alpha}\right) - \frac{B}{\alpha} \tag{A.2}$$

$$\mathcal{P}_J = -\frac{1}{2\sigma^2}(\log(J) - \log(J_0))^2 - \log(J)\ln(10) \tag{A.3}$$

with $S$ being the expected number of signal events, $B$ the number of expected background events, $J$ the expected astrophysical factor, $n_{On}$ the number of observed events in the signal region, $n_{Off}$ the number of events observed in the background region, $\alpha$ the scaling factor between the signal and background region and $J_0$ the assumed astrophysical factor. log is the logarithm for base 10 and ln the logarithm for base $e$. Note that all additive constants are dropped here because they will not change the derivatives and the profile-likelihood later on.
To optimize the log-likelihood means optimizing the parameters $B$ and $J$ for a given velocity averaged annihilation factor $\langle\sigma v\rangle$. It it important to note that $S \propto \langle\sigma v\rangle\, 10^{\log(J)} = \langle\sigma v\rangle\, e^{J\ln(10)}$ and therefore the Equations A.1 and A.3 are coupled making the estimation of an optimal $B$ value dependent on the estimation of an optimal $\log(J)$ value and vice versa.
The derivatives needed are therefore:

$$\mathcal{P}_b'(B) + \mathcal{P}_s'(B) = \mathcal{P}'(B) = \frac{n_{On}}{S+B} + \frac{n_{Off}}{B} - \left(1 + \frac{1}{\alpha}\right) \tag{A.4}$$

and

$$\begin{aligned}&\mathcal{P}'_s(\log(J)) + \mathcal{P}'_J(\log(J)) = \\ &\mathcal{P}'(\log(J)) = S\ln(10)\left[\frac{n_{On}}{S+B} - 1\right] - \frac{\log(J) - \log(J_0)}{\sigma^2} - \ln(10).\end{aligned} \tag{A.5}$$

Where $\mathcal{P}'(x)$ denotes $\partial\mathcal{P}/\partial x$. To optimize the coupled Equations an iterative numerical approach is used. First Equation A.4 will be solved for B for a preliminary estimation of $\log(J)$. In the first iteration the preliminary estimation $\log(J) = \log(J_0)$ is used. Then Equation A.5 is optimized for the value of $B$ obtained in the previous step. After that the new value of $\log(J)$ will be used to optimize $B$ again. These steps are repeated until the old and new values of $B$ and $\log(J)$ do not change any more.
The optimal value in each iteration is calculated using the Newton method to find the root of the derivatives. The derivative needed for the Newton's method for Equation A.4 is:

$$\mathcal{P}''(B) = -\frac{n_{On}}{(S+B)^2} - \frac{n_{Off}}{B^2} \tag{A.6}$$

and for Equation A.5:

$$\mathcal{P}''(\log(J)) = S\ln^2(10)\left[B\frac{n_{On}}{(S+B)^2} - 1\right] - \frac{1}{\sigma^2}. \tag{A.7}$$

As starting value for the Newton method $B = n_{Off}\alpha$ and $\log(J) = \log(J_0)$ are used assuming that the optimal values for a given $\langle\sigma v\rangle$ are close to the overall optimal values, see Chapter 4.

# Appendix B

# Hardware Integration And Control Software for the CTA Midium-Size Telescope Prototype

**Figure B.1:** The MST prototype in Adlershof, Berlin.

In 2013 the MST prototype started operation in Adlershof, Berlin. One of the tasks to be investigated with the MST is to assure that the steel structures rigidity is high enough to ensure exact pointing for observations. For that purpose the correlation of local weather data, like wind speed and temperature, and the bending of the steal structure will be studied. A Davis Vantage Vue, see Figure B.4, Weather Station (WS) is installed on a lightning rod close to the MST to provide the data. For specifications see [96]. This weather station had to be included in the CTA control software and the data taken had to be stored.
The following sections will describe the prototype, the software environment and the implementation of the weather station into the software environment.

## B.1 The Medium Sized Telescope Prototype

The prototype has a modified Davis-Cotton design reflector [97] with a focal length of 16 m and a dish diameter of 12 m. A picture of the prototype can be seen in Figure B.1. The dish is equipped with real and dummy mirrors. While the dummy mirrors just emulate the weight of real mirrors, the real mirrors will be used to test the alignment procedures using Active Mirror Controls (AMCs).
Berlin's high background light level makes any gamma-ray astronomy impossible, therefore no PMT camera is installed on the prototype. To emulate the weight of a PMT camera a dummy camera with a weight of 2.5 t is installed on the prototype.
Furthermore the prototype has a drive system so that the prototype can be steered to any position at the sky. Three Charged-Coupled Device (CCD) cameras on the structure are used to observe the behaviour of the structure in different pointing positions under different weather conditions.

## B.2 OPC Unified Architecture

OPC Unified Architecture (OPC UA) [98] is a well known set of standards that allow unified access to hardware devices. The use of OPC UA was decided to ensure easy, unified access and easy maintenance of hardware components as well as easy installation of new hardware. OPC UA is foreseen to be a middle layer between hardware and the control framework ALMA Common Software (ACS) (see following section).
OPC UA is platform independent, meaning OPC UA servers do not have

to run on the same operating system as the clients. Servers and clients can be programmed in C++, Java and Microsoft.net, giving developers flexibility. The functionalities of a OPC UA server include alarms, subscriptions, method calls and nodes. Nodes are access points in an OPC UA server, for example a variable. In general it is foreseen to use only method calls and nodes for data access in the MST prototype.
For the WS an OPC UA server had to be written because the Davis Ventage Vue does not come with an OPC UA server. The server was written by David Melkumyan using the Java SDK from Prosys [99].

## B.3 ALMA Common Software

ACS is a CORBA based software framework designed for the Atacama Large Millimeter/submillimeter Array (ALMA) observatory [100] to control the 66 radio telescopes and all subsystems that are in the experiment. The ACS framework is based on a container-component model [101] and allows to write components in C++, Java and Python allowing for easy software development and maintainability.
ACS comes with many services important for a large scale experiment like a logging and alarm system. For more details on the structure of ACS see [102]. The complexity of CTA is on the same level as ALMA. Therefore ACS is considered as control software for CTA. The MST prototype is a good testbench for the control software and therefore ACS is used to control all parts of the MST including auxiliaries like the WS.

## B.4 Sqlalchemy

For future analysis weather data must be stored. It is clear that a relational (table based) Data Base (DB) is an appropriate solution for the small amount of data a weather station produces. Important for the selection of the DB was easy storage from ACS and easy query of archived data. Therefore it was decided to investigate MySql combined with Sqlalchemy [103]. Sqlalchemy is a Python package that makes building an Object Relation Mapper (ORM) and query data with the ORM easy. Sqlalchemy being Python based makes it possible to include the code for data storage directly in ACS or to write scripts that connect to ACS and store data.
Two designs were proposed for the MySQL DB, a traditional and a compact design. UML class diagrams describing both designs can be seen in Figure B.2 and Figure B.3. Each box in the Unified Modeling Language (UML)

class diagram represents a table in the MySQL DB. The lines connecting boxes indicate a relation between table entries in different tables. The traditional schema used here has six tables for different value types which are int_property_value, float_property_value, enum_property_value, bit_field_property_value, text_property_value and structured_property_value. Each value table contains the value of the property (value) and a corresponding time stamp (tm). Additional at the same level as the value tables a log table containing logging information as well as the time stamps indicating when the conditions were raised and solved (start_tm and stop_tm) and if logging is enabled for the property (enabled). These tables also contain a relation to the property table with property_id, indicating which property the value is related to. As example, values for wind speed and temperature will be stored both in the float_property_value but will point to different property entries via property_id. The property table contains the description of the different properties (name). The table has two relation links to two tables. The first one is the link to property_type which contains information about the property type, for example if the property is a monitored read only value such as weather data or if it is a controllable read and write value like pointing position. The second table the property table is linked to is the component table which contains the unique component name the property comes from. Finally the component table as a relational link to the component_type table giving the type of the component.
The compact schema is similar to the traditional schema. It is missing the component and component_type tables. The information about the component and the component type is directly stored in the property table producing more overhead.

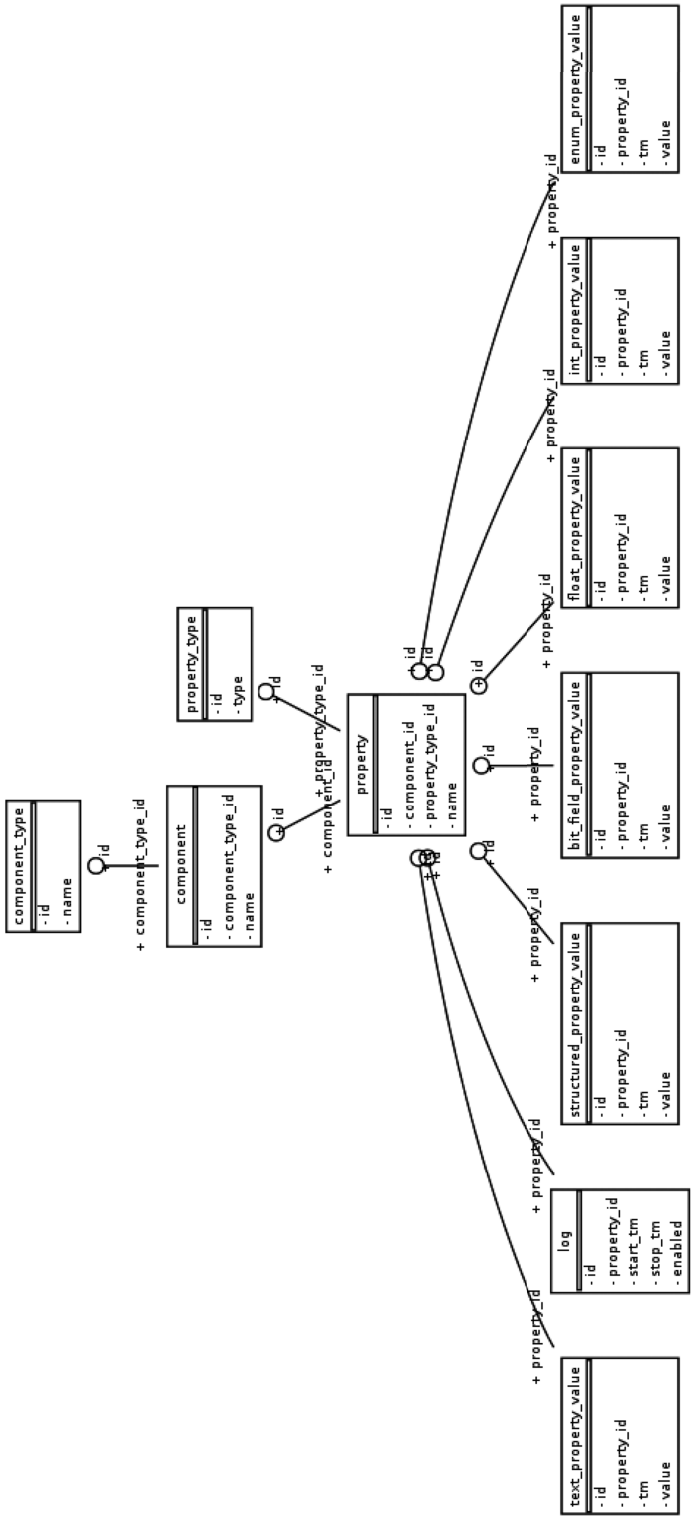


**Figure B.2:** UML class diagram of the traditional schema for the MySQL database for the MST. Each box is a table in the DB and the lines show relations between tables. See the text for a description of the individual tables and their content.

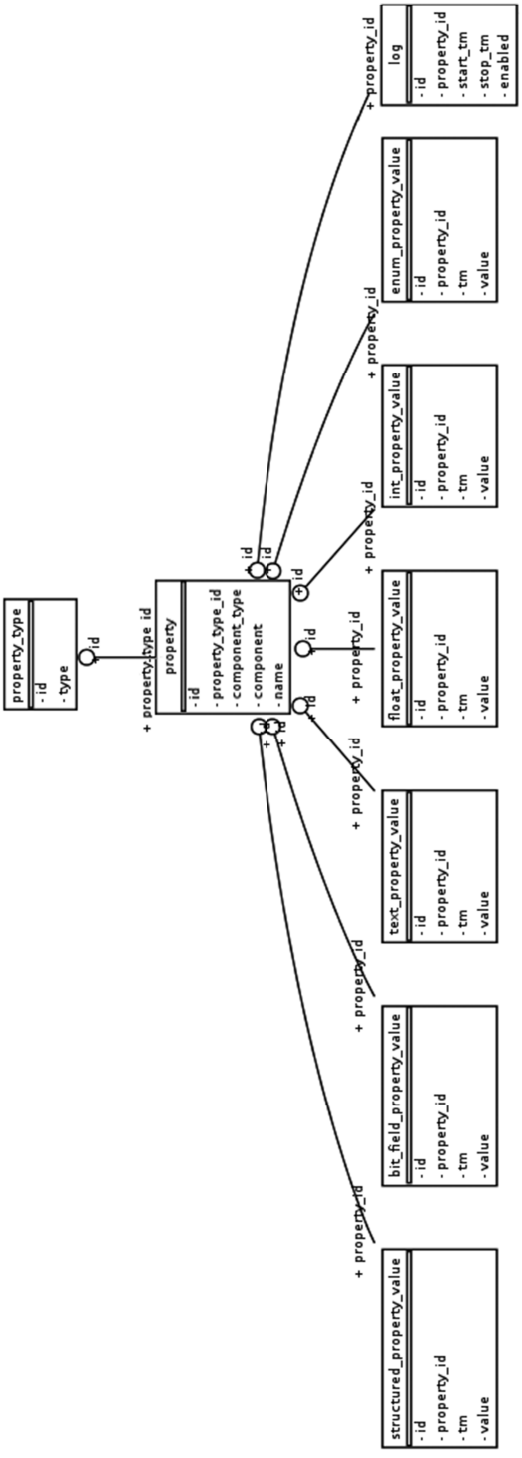


**Figure B.3:** UML class diagram of the compact schema for a MySQL database. Each box is a table in the DB and the lines show relations between tables. See the text for a description of the individual tables and their content.

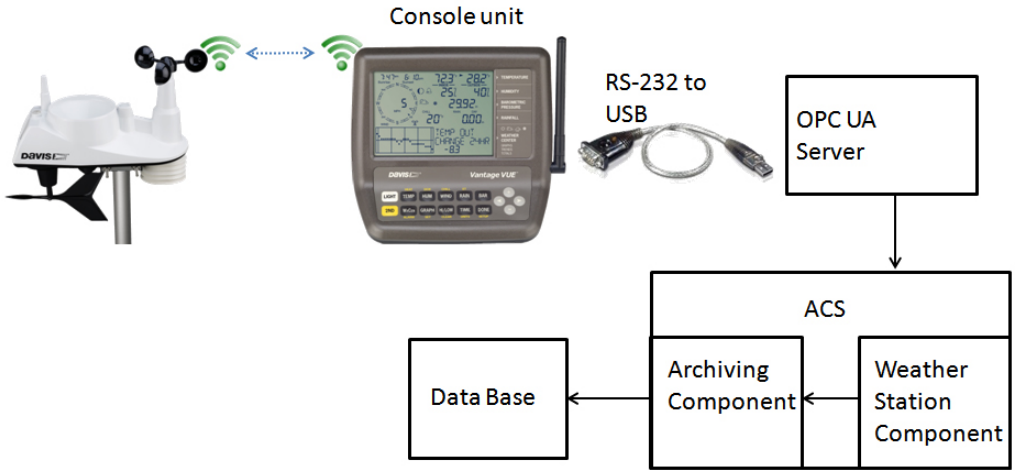


**Figure B.4:** The WS is communicating with the console unit via wireless connection. The console is connected to the OPC UA server via a RS-232 to USB converter. Through the network an ACS component which works as an OPC UA client gets the weather data. The archiving component then stores the data in a DB.

## B.5 Connecting The Weather Station

The weather station outdoor unit communicates with the console unit via wireless communication with 868.0-868.6 MHz Frequency Hopping Spread Spectrum (FHSS). FHSS is a wireless communication system which changes the carrier frequency according to a pseudo-random sequence ensuring resistance to narrowband interferences [104]. The range of the wireless communication is 300 m with direct line of sight and 60 to 120 m through walls. The console has a serial line to connect to a PC. The WS measures:

- inside & outside temperature
- inside & outside humidity
- atmospheric pressure
- rain rate
- wind speed
- wind direction.

For the specifications see [105].
Because newer PC often miss a serial interface a RS-232 to USB Serial adapter is used. The PC is running an OPC UA server. The server uses the serial protocol given by the producer [106]. The bytes follow the least significant byte first order for multi byte values.
Over the network an ACS component acting as an OPC UA client can access

the server. The WS component is an ACS Java component. On start-up, the component connects to the OPC UA WS server and accesses the nodes containing the weather data and provides the data to the rest of the data acquisition and control system as ACS properties.
The server address as well as the nodes addresses are defined in an xml file. The connection to the server is managed by a Java package written by David Melkumyan.
As a last step, an archiving component in the ACS system reads out all the values in regular intervals and stores them in a DB for later use. See Figure B.4 for a schematic view of the connections.

# Bibliography


[1] Matts Roos. Dark Matter: The evidence from astronomy, astrophysics and cosmology. 2010, arXiv: 1001.0316.

[2] F. Zwicky. Die Rotverschiebung von extragalaktischen Nebeln. *Helvetica Physica Acta*, 6:110–127, 1933.

[3] Alexandre Refregier. Weak gravitational lensing by large scale structure. *Ann.Rev.Astron.Astrophys.*, 41:645–668, 2003, astro-ph/0307212.

[4] Douglas Clowe, Marusa Bradac, Anthony H. Gonzalez, Maxim Markevitch, Scott W. Randall, et al. A direct empirical proof of the existence of dark matter. *Astrophys.J.*, 648:L109–L113, 2006, astro-ph/0608407.

[5] K. G. Begeman, A. H. Broeils, and R. H. Sanders. Extended rotation curves of spiral galaxies - Dark haloes and modified dynamics. *MNRAS*, 249:523–537, April 1991.

[6] P.A.R. Ade et al. Planck 2013 results. XVI. Cosmological parameters. 2013, arXiv: 1303.5076.

[7] L. Wyrzykowski, J. Skowron, S. Kozlowski, A. Udalski, M.K. Szymanski, et al. The OGLE View of Microlensing towards the Magellanic Clouds. IV. OGLE-III SMC Data and Final Conclusions on MACHOs. 2011, 1106.2925.

[8] M. Milgrom. A Modification of the Newtonian dynamics as a possible alternative to the hidden mass hypothesis. *Astrophys.J.*, 270:365–370, 1983.

[9] Bringman J. and et. al. *Phys. Rev. D.*, 86, 2012.

[10] R. D. Peccei and Helen R. Quinn. Cp. *Phys. Rev. Lett.*, 38:1440–1443, Jun 1977.

[11] Leslie J Rosenberg and Karl A. van Bibber. Searches for invisible axions. *Physics Reports*, 325(1):1 – 39, 2000.

[12] Miguel A. Sanchez-Conde, David Paneque, Elliott D. Bloom, Francisco Prada, and Alberto Dominguez. The Search of Axion-Like-Particles with Fermi and Cherenkov Telescopes. 2010, arXiv: 1001.1892.

[13] Alessandro De Angelis, Giorgio Galanti, and Marco Roncadelli. Relevance of axion-like particles for very-high-energy astrophysics. *Phys.Rev.*, D84:105030, 2011, arXiv: 1106.1132.

[14] Paolo Panci. New Directions in Direct Dark Matter Searches. *Adv.High Energy Phys.*, 2014:681312, 2014, 1402.1507.

[15] Paolo Beltrame. Direct Dark Matter search with the XENON program. 2013, arXiv: 1305.2719.

[16] R. Bernabei, P. Belli, S. d'Angelo, A. Di Marco, F. Montecchia, et al. Dark Matter investigation by DAMA at Gran Sasso. *International Journal of Modern Physics A*, 28:1330022, 2013, arXiv: 1306.1411.

[17] Mathias Garny, Alejandro Ibarra, Miguel Pato, and Stefan Vogl. On the spin-dependent sensitivity of XENON100. *Phys.Rev.*, D87:056002, 2013, arXiv: 1211.4573.

[18] Christopher Savage, Paolo Gondolo, and Katherine Freese. Can WIMP spin dependent couplings explain DAMA data, in light of null results from other experiments? *Phys.Rev.*, D70:123513, 2004, astro-ph/0408346.

[19] C.E. Aalseth et al. CoGeNT: A Search for Low-Mass Dark Matter using p-type Point Contact Germanium Detectors. 2012, arXiv: 1208.5737.

[20] Oscar Adriani et al. An anomalous positron abundance in cosmic rays with energies 1.5-100 GeV. *Nature*, 458:607–609, 2009, arXiv: 0810.4995.

[21] M. Ackermann et al. Measurement of separate cosmic-ray electron and positron spectra with the Fermi Large Area Telescope. *Phys.Rev.Lett.*, 108:011103, 2012, arXiv: 1109.0521.

[22] Marco Cirelli. Indirect Searches for Dark Matter: a status review. *Pramana*, 79:1021–1043, 2012, arXiv: 1202.1454.

[23] Pasquale D. Serpico. Astrophysical models for the origin of the positron 'excess'. *Astropart.Phys.*, 39-40:2–11, 2012, arXiv: 1108.4827.

[24] M.G. Aartsen, R. Abbasi, Y. Abdou, M. Ackermann, J. Adams, et al. An IceCube Search for Dark Matter Annihilation in nearby Galaxies and Galaxy Clusters. 2013, 1307.3473.

[25] S. Adrian-Martinez et al. First Search for Dark Matter Annihilation in the Sun Using the ANTARES Neutrino Telescope. 2013, 1302.6516.

[26] Elmo Tempel, Andi Hektor, and Martti Raidal. Fermi 130 GeV gamma-ray excess and dark matter annihilation in sub-haloes and in the Galactic centre. *JCAP*, 1209:032, 2012, arXiv: 1205.1045.

[27] J.A.R. Cembranos, A. de la Cruz-Dombriz, A. Dobado, R.A. Lineros, and A.L. Maroto. Photon spectra from WIMP annihilation. *Phys.Rev.*, D83:083507, 2011, arXiv: 1009.4936.

[28] Argyro Tasitsiomi and A.V. Olinto. The Detectability of neutralino clumps via atmospheric Cherenkov telescopes. *Phys.Rev.*, D66:083006, 2002, astro-ph/0206040.

[29] Alan R. Duffy, Joop Schaye, Scott T. Kay, Claudio Dalla Vecchia, Richard A. Battye, and C. M. Booth. Impact of baryon physics on dark matter structures: a detailed simulation study of halo density profiles. *Monthly Notices of the Royal Astronomical Society*, 405(4):2161–2178, 2010.

[30] Susana E. Pedrosa, Patricia B. Tissera, and Cecilia Scannapieco. Effects of SN Feedback on the Dark Matter Distribution. 2008, 0807.2548.

[31] D. Heath Jones, Mike A. Read, Will Saunders, Matthew Colless, Tom Jarrett, et al. The 6dF Galaxy Survey: Final Redshift Release (DR3) and Southern Large-Scale Structures. 2009, arXiv: 0903.5451.

[32] Julio F. Navarro, Carlos S. Frenk, and Simon D.M. White. The Structure of cold dark matter halos. *Astrophys.J.*, 462:563–575, 1996, astro-ph/9508025.

[33] Julio F. Navarro, Carlos S. Frenk, and Simon D. M. White. A universal density profile from hierarchical clustering. *The Astrophysical Journal*, 490(2):493, 1997.

[34] Carlos A. Vera-Ciro, Amina Helmi, Else Starkenburg, and Maarten A. Breddels. Not too big, not too small: the dark halos of the dwarf spheroidals in the Milky Way. 2012, arXiv: 1202.6061.

[35] Dan Coe. Dark Matter Halo Mass Profiles. 2010, arXiv: 1005.0411.

[36] G. D. Martinez. A Robust Determination of Milky Way Satellite Properties using Hierarchical Mass Modeling. *ArXiv e-prints*, September 2013, 1309.2641.

[37] V. Springel, S.D.M. White, C.S. Frenk, J.F. Navarro, A. Jenkins, et al. Prospects for detecting supersymmetric dark matter in the Galactic halo. *Nature*, 456N7218:73–80, 2008.

[38] V. F. Hess. Über beobachtungen der durchdringenden strahlung bei sieben freiballonfahrten. *Phys. Zeitschr.*, XIII:1084, 1912.

[39] P. Morrison. On gamma-ray astronomy. *Il Nuovo Cimento*, 7(6):858–865, 1958.

[40] W. L. Kraushaar and G. W. Clark. Search for primary cosmic gamma rays with the satellite explorer xi. *Phys. Rev. Lett.*, 8:106–109, Feb 1962.

[41] T. C. Weekes, C. W. Akerlof, M. Chantell, E. Colombo, M. F. Cawley, V. Connaughton, D. J. Fegan, S. Fennell, J. Gaidos, A. M. Hillas, A. D. Kerrick, P. Kwok, D. A. Lewis, R. C. Lamb, D. I. Meyer, G. Mohanty, J. Rose, A. Rovero, G. Sembroski, M. S. Schubnell, M. Punch, M. West, T. Whitaker, and C. Wilson. Observations of the crab nebula at tev energies. *AIP Conference Proceedings*, 304(1):270–274, 1994.

[42] ENRICO Fermi. On the origin of the cosmic radiation. *Phys. Rev.*, 75:1169–1174, Apr 1949.

[43] Frank M. Rieger, Emma de Ona-Wilhelmi, and Felix A. Aharonian. TeV Astronomy. 2013, 1302.5603.

[44] Luigi Piro, Livio Scarsi, and R. C. Butler. Sax: the wideband mission for x-ray astronomy, 1995.

[45] E. Costa, F. Frontera, J. Heise, M. Feroci, Jean J.M. in 't Zand, et al. Discovery of an X-ray afterglow associated with the gamma-ray burst of 28 February 1997. *Nature*, 387:783–785, 1997, astro-ph/9706065.

[46] H. Tajima, f. t. Fermi LAT, and Fermi GBM collaborations. Fermi Observations of high-energy gamma-ray emissions from GRB 080916C. *ArXiv e-prints*, July 2009, 0907.0714.

[47] S.E. Woosley and J.S. Bloom. The Supernova Gamma-Ray Burst Connection. *Ann.Rev.Astron.Astrophys.*, 44:507–556, 2006, astro-ph/0609142.

[48] K.I. Kellermann, Y.Y. Kovalev, M.L. Lister, D.C. Homan, M. Kadler, et al. Doppler Boosting, Superluminal Motion, and the Kinematics of AGN Jets. *Astrophys.Space Sci.*, 311:231–239, 2007, 0708.3219.

[49] Robert J. Gould and Gérard P. Schréder. Opacity of the universe to high-energy photons. *Phys. Rev.*, 155:1408–1411, Mar 1967.

[50] Pierre Brun and Denis Wouters. Constraints on axion-like particles with H.E.S.S. from observations of PKS 2155-304. 2013, 1307.6068.

[51] Alexander Heger, C.L. Fryer, S.E. Woosley, N. Langer, and D.H. Hartmann. How massive single stars end their life. *Astrophys.J.*, 591:288–300, 2003, astro-ph/0212469.

[52] M. Ackermann et al. Detection of the Characteristic Pion-Decay Signature in Supernova Remnants. *Science*, 339:807, 2013, 1302.3307.

[53] W. Heitler. *The Quantum Theory of Radiation*. Dover Books on Physics and Chemistry. Dover Publications, 1954.

[54] P. A. Čerenkov. Visible radiation produced by electrons moving in a medium with velocities exceeding that of light. *Phys. Rev.*, 52:378–379, Aug 1937.

[55] http://upload.wikimedia.org/wikipedia/commons/thumb/6/6b/Cherenkov.svg/1103px-Cherenkov.svg.png.

[56] Werner Hofmann. Results from HESS. *eConf*, C040802:THT004, 2004.

[57] F. Aharonian et al. Observations of the Crab Nebula with H.E.S.S. *Astron.Astrophys.*, 457:899–915, 2006, astro-ph/0607333.

[58] Wystan Benbow and H.E.S.S. Collaboration. The status and performance of h.e.s.s. *AIP Conference Proceedings*, 745(1):611–616, 2005.

[59] Stefan Funk, G. Hermann, J. Hinton, D. Berge, K. Bernlohr, et al. The Trigger system of the H.E.S.S. Telescope array. *Astropart.Phys.*, 22:285–296, 2004, astro-ph/0408375.

[60] Andreas Hocker, J. Stelzer, F. Tegenfeldt, H. Voss, K. Voss, et al. TMVA - Toolkit for Multivariate Data Analysis. *PoS*, ACAT:040, 2007, physics/0703039.

[61] S. Ohm, C. van Eldik, and K. Egberts. Gamma-Hadron Separation in Very-High-Energy gamma-ray astronomy using a multivariate analysis method. *Astropart.Phys.*, 31:383–391, 2009, 0904.1136.

[62] A.M. Hillas. In *Proceedings of the 19th International Cosmic Ray Conference*, volume 3, page 445, 1985.

[63] A. Abramowski et al. H.E.S.S. constraints on Dark Matter annihilations towards the Sculptor and Carina Dwarf Galaxies. *Astropart.Phys.*, 34:608–616, 2011, arXiv: 1012.5602.

[64] E. Moulin et al. Search for a Dark Matter annihilation signal from the Sagittarius dwarf galaxy with H.E.S.S. 2007, arXiv: 0711.3682.

[65] G. Lamanna, C. Farnier, A. Jacholkowska, and M. Kieffer. Sagittarius dwarf spheroidal galaxy observed by H.E.S.S. 2013, 1307.4918.

[66] Joe Wolf, Gregory D. Martinez, James S. Bullock, Manoj Kaplinghat, Marla Geha, Ricardo R. Muñoz, Joshua D. Simon, and Frank F. Avedo. Accurate masses for dispersion-supported galaxies. *Monthly Notices of the Royal Astronomical Society*, 406(2):1220–1237, 2010.

[67] Matthew G. Walker, Mario Mateo, Edward W. Olszewski, Jorge Peñarrubia, N. Wyn Evans, and Gerard Gilmore. A universal mass profile for dwarf spheroidal galaxies? *The Astrophysical Journal*, 704(2):1274, 2009.

[68] Wolfgang A. Rolke and Angel M. Lopez. Confidence intervals and upper bounds for small signals in the presence of background noise. *Nucl.Instrum.Meth.*, A458:745–758, 2001, hep-ph/0005187.

[69] S. S. Wilks. The large-sample distribution of the likelihood ratio for testing composite hypotheses. *The Annals of Mathematical Statistics*, 9(1):pp. 60–62, 1938.

[70] Lars Bergström, Piero Ullio, and James H. Buckley. Observability of $\gamma$ rays from dark matter neutralino annihilations in the milky way halo. *Astroparticle Physics*, 9(2):137 – 162, 1998.

[71] K. V. Johnston, D. N. Spergel, and L. Hernquist. The Disruption of the Sagittarius Dwarf Galaxy. *apj*, 451:598, October 1995, astro-ph/9502005.

[72] M. Llena Garde, J. Conrad, J. Cohen-Tanugi, for the Fermi-LAT collaboration, M. Kaplinghat, and G. Martinez. Constraining Dark Matter Signal from a Combined Analysis of Milky Way Satellites with the Fermi-LAT. *ArXiv e-prints*, November 2011, 1111.0320.

[73] The fermi large area telescope. `http://www-glast.stanford.edu/`.

[74] W. B. Atwood, A. A. Abdo, M. Ackermann, W. Althouse, B. Anderson, M. Axelsson, L. Baldini, J. Ballet, D. L. Band, G. Barbiellini, and et al. The Large Area Telescope on the Fermi Gamma-Ray Space Telescope Mission. *apj*, 697:1071–1102, June 2009, 0902.1089.

[75] A. Charbonnier, C. Combet, M. Daniel, S. Funk, J. A. Hinton, D. Maurin, C. Power, J. I. Read, S. Sarkar, M. G. Walker, and M. I. Wilkinson. Dark matter profiles and annihilation in dwarf spheroidal galaxies: prospectives for present and future $\gamma$-ray observatories - I. The classical dwarf spheroidal galaxies. *mnras*, 418:1526–1556, December 2011, 1104.0412.

[76] M. Ackermann, M. Ajello, A. Albert, and et. al. The Fermi Large Area Telescope on Orbit: Event Classification, Instrument Response Functions, and Calibration. *apjs*, 203:4, November 2012, 1206.1896.

[77] A. Abramowski and et. al. Search for a Dark Matter Annihilation Signal from the Galactic Center Halo with H.E.S.S. *Physical Review Letters*, 106(16):161301, April 2011, 1103.3266.

[78] M. Doro et al. Dark Matter and Fundamental Physics with the Cherenkov Telescope Array. *Astropart.Phys.*, 43:189–214, 2013, arXiv: 1208.5356.

[79] K. Bernlöhr, A. Barnacka, Y. Becherini, O. Blanch Bigas, E. Carmona, P. Colin, G. Decerprit, F. Di Pierro, F. Dubois, C. Farnier, S. Funk, G. Hermann, J. A. Hinton, T. B. Humensky, B. Khélifi, T. Kihm, N. Komin, J.-P. Lenain, G. Maier, D. Mazin, M. C. Medina, A. Moralejo, S. J. Nolan, S. Ohm, E. de Oña Wilhelmi, R. D. Parsons, M. Paz Arribas, G. Pedaletti, S. Pita, H. Prokoph, C. B. Rulten, U. Schwanke, M. Shayduk, V. Stamatescu, P. Vallania, S. Vorobiov, R. Wischnewski, T. Yoshikoshi, A. Zech, and CTA Consortium. Monte

Carlo design studies for the Cherenkov Telescope Array. *Astroparticle Physics*, 43:171–188, March 2013, 1210.3503.

[80] Volker Springel, Jie Wang, Mark Vogelsberger, Aaron Ludlow, Adrian Jenkins, et al. The Aquarius Project: the subhalos of galactic halos. *Mon.Not.Roy.Astron.Soc.*, 391:1685–1711, 2008, arXiv: 0809.0898.

[81] J. Diemand, M. Kuhlen, P. Madau, M. Zemp, B. Moore, et al. Clumps and streams in the local dark matter distribution. *Nature*, 454:735–738, 2008, arXiv: 0805.1244.

[82] F. Aharonian, , et al. Spectrum and variability of the Galactic Center VHE gamma-ray source HESS J1745-290. *Astron.Astrophys.*, 503:817, 2009, arXiv: 0906.1247.

[83] Q. D. Wang, F. J. Lu, and E. V. Gotthelf. G359.95-0.04: an energetic pulsar candidate near Sgr A*. *Monthly Notices of the Royal Astronomical Society*, 367(3):937–944, 2006.

[84] F. Aharonian et al. Discovery of very-high-energy gamma-rays from the galactic centre ridge. *Nature*, 439:695–698, 2006, astro-ph/0603021.

[85] A.M. Hillas. *Proc. 19th ICRC*, 3:445, 1985.

[86] (MAGIC Collaboration) J. Albert et. al. Implementation of the Random Forest method for the Imaging Atmospheric Cherenkov Telescope MAGIC. *Nuclear Instruments and Methods in Physics Research Section A: Accelerators, Spectrometers, Detectors and Associated Equipment*, 588(3):424 – 432, 2008.

[87] K. Bernlöhr, A. Barnacka, Y. Becherini, O. Blanch Bigas, E. Carmona, P. Colin, G. Decerprit, F. Di Pierro, F. Dubois, C. Farnier, S. Funk, G. Hermann, J.A. Hinton, T.B. Humensky, B. Khélifi, T. Kihm, N. Komin, J.-P. Lenain, G. Maier, D. Mazin, M.C. Medina, A. Moralejo, S.J. Nolan, S. Ohm, E. de Oña Wilhelmi, R.D. Parsons, M. Paz Arribas, G. Pedaletti, S. Pita, H. Prokoph, C.B. Rulten, U. Schwanke, M. Shayduk, V. Stamatescu, P. Vallania, S. Vorobiov, R. Wischnewski, T. Yoshikoshi, and A. Zech. Monte carlo design studies for the cherenkov telescope array. *Astroparticle Physics*, 43(0):171 – 188, 2013.

[88] M. Actis et al. Design concepts for the Cherenkov Telescope Array CTA: An advanced facility for ground-based high-energy gamma-ray astronomy. *Exper.Astron.*, 32:193–316, 2011, 1008.3703.

[89] A. Abramowski et al. Search for a Dark Matter annihilation signal from the Galactic Center halo with H.E.S.S. *Phys.Rev.Lett.*, 106:161301, 2011, arXiv: 1103.3266.

[90] T.-P. Li and Y.-Q. Ma. Analysis methods for results in gamma-ray astronomy. *APJ*, 272:317–324, September 1983.

[91] Paolo Gondolo and Joseph Silk. Dark matter annihilation at the galactic center. *Phys. Rev. Lett.*, 83:1719–1722, Aug 1999.

[92] W. A. Rolke, A. M. López, and J. Conrad. Limits and confidence intervals in the presence of nuisance parameters. *Nuclear Instruments and Methods in Physics Research A*, 551:493–503, October 2005, arXiv: physics/0403059.

[93] Torsten Bringmann, Lars Bergstrom, and Joakim Edsjo. New Gamma-Ray Contributions to Supersymmetric Dark Matter Annihilation. *JHEP*, 0801:049, 2008, arXiv: 0710.3169.

[94] Ze-Peng Liu, Yue-Liang Wu, and Yu-Feng Zhou. Sommerfeld enhancements with vector, scalar and pseudoscalar force-carriers. 2013, arXiv: 1305.5438.

[95] M. Doro, J. Conrad, D. Emmanoulopoulos, M. A. Sànchez-Conde, J. A. Barrio, E. Birsin, J. Bolmont, P. Brun, S. Colafrancesco, S. H. Connell, J. L. Contreras, M. K. Daniel, M. Fornasa, M. Gaug, J. F. Glicenstein, A. González-Muñoz, T. Hassan, D. Horns, A. Jacholkowska, C. Jahn, R. Mazini, N. Mirabal, A. Moralejo, E. Moulin, D. Nieto, J. Ripken, H. Sandaker, U. Schwanke, G. Spengler, A. Stamerra, A. Viana, H.-S. Zechlin, S. Zimmer, and CTA Consortium. Dark matter and fundamental physics with the Cherenkov Telescope Array. *Astroparticle Physics*, 43:189–214, March 2013, 1208.5356.

[96] Vantage vue weather station specification sheet. `http://www.vantagevue.com/product_documents/weather/spec_sheets/6250_6351_57_SS.pdf`.

[97] John M. Davies and Eugene S. Cotton. Design of the quartermaster solar furnace. *Solar Energy*, 1(2–3):16 – 22, 1957. ¡ce:title¿The Proceedings of the Solar Furnace Symposium ¡/ce:title¿.

[98] Opc foundation main web page. `https://www.opcfoundation.org`.

[99] Prosys main web page. http://www.prosysopc.com/opc-ua-java-sdk.php.

[100] Alma main web page. http://www.almaobservatory.org.

[101] M. Völter, A. Schmid, and E. Wolff. *Server Component Patterns: Component Infrastructures Illustrated with EJB*. Wiley Software Patterns Series. Wiley, 2003.

[102] G. Chiozzi, B. Gustafsson, B. Jeram, P. Sivera, M. Plesko, et al. Common software for the ALMA project. *eConf*, C011127:THAT005, 2001, physics/0111034.

[103] Sqlalchemy main web page. http://www.sqlalchemy.org/.

[104] American National Standard. *Telecom Glossary 2000 T1.523-2001*, 2001. "http://www.atis.org/tg2k/".

[105] Davis vantage vue specification sheet. http://www.davisnet.com/product_documents/weather/spec_sheets/6250_6351_57_SS.pdf.

[106] Weather station serial protocol. http://www.davisnet.com/support/weather/download/VantageSerialProtocolDocs_v261.pdf.

# List of Acronyms

**FoV** Field of View

**DM** Dark Matter

**WIMP** Weakly Interacting Massive Particle

**CTA** Cherenkov Telescope Array

**H.E.S.S.** High Energy Spectroscopic System

**MST** Medium Sized Telescope

**GC** Galactic Center

**VHE** Very High Energy

**GRB** Gamma-Ray Burst

**los** line of sight

**CMB** Cosmic Microwave Background

**IACT** Imaging Atmospheric Cherenkov Telescope

**ACS** ALMA Common Software

**OPC UA** OPC Unified Architecture

**FHSS** Frequency Hopping Spread Spectrum

**BDT** Boosted Decision Tree

**VHE** Very High Energy ($E \geq 100\,\mathrm{GeV}$)

**MAGIC** Major Atmospheric Imaging Cherenkov Telescope

**DB** Data Base

**TMVA** Toolkit for MultiVariate Analysis

**IC** Inverse Compton

**p.e.** photoelectrons

**EBL** Extragalactic Background Light

**UML** Unified Modeling Language

**CR** Cosmic Ray

**ToO** Target of Opportunity

**AGN** Active Galactic Nucleus

**HAP** HESS Analysis Program

**ORM** Object Relation Mapper

**MVA** MultiVariate Analysis

**MRSW** Mean Reduced Scaled Width

**MRSL** Mean Reduced Scaled Length

**Fermi LAT** Fermi Large Area Telescope

**mSUGRA** minimal Super Gravity

**MRSLO** Mean Reduced Scaled Length Off

**MRSWO** Mean Reduced Scaled Width Off

**ISM** Inter Stellar Medium

**SM** Standard Model

**SUSY** Supersymmetry

**MOND** Modified Newtonian Dynamics

**ALMA** Atacama Large Millimeter/submillimeter Array

**PMT** Photo Multiplier Tube

**NSB** Night Sky Background

**NFW** Navarro-Frenk-White

**LST** Large Size Telescope

**SST** Small Size Telescope

**MACHO** Massive Compact Halo Objects

**MC** Monte Carlo

**DAMA** Dark Matter

**AMC** Active Mirror Control

**RF** Random Forest

**cMSSM** Constrained Minimal Supersymmetric Extension of the Standard Model

**LHC** Large Hadron Collider

**TCP** Time-Projection Chamber

**LSP** Lightest Super-Symmetric Particle

**WS** Weather Station

**CCD** Charged-Coupled Device

# List of Figures

# List of Tables

# Acknowledgements

I want to thank my family and especially my parents for their support throughout the years. My colleagues for their help and the inspiring conversations. Furthermore I want to thank my supervisor Ullrich Schwanke for all the prove reading. Also thanks to all my friends who gave me needed distractions.

# Selbstständigkeitserklärung zur Dissertation

Hiermit versichere ich, Emrah Birsin, dass die vorliegende Dissertation selbständig und nur unter Verwendung der angegebenen Literatur und Hilfsmittel angefertigt wurde.

Berlin, den Emrah Birsin